Mineral Dust and Pedogenesis in the Alpine Critical Zone

Munroe, Jeffrey S.[1], Santis, Abigail A.[1], Soderstrom, Elsa J.[1], Tappa, Michael J.[2], Bauer, Ann M.[2]

[1]Department of Earth & Climate Sciences, Middlebury College, Middlebury, VT 05753, USA
[2]Department of Geoscience, University of Wisconsin-Madison, Madison, WI 53706, USA

Correspondence to: Jeffrey S. Munroe (jmunroe@middlebury.edu)

Abstract. The influence of mineral dust deposition on soil formation in the mountain critical zone was evaluated at six sites in southwestern North America. Passive samplers collected dust for two years, and representative soil and rock were gathered in the vicinity of each dust sampler. All materials (dust, soil, and rock) were analysed to determine their mineralogy (with x-ray diffraction), geochemistry (with ICP-MS), and radiogenic isotope fingerprint ($^{87}Sr/^{86}Sr$ and ε_{Nd}). In addition, the grain size distribution of dust and soil samples was determined with laser scattering, and standard soil fertility analysis was conducted on the soil samples. Results reveal that minerals present in the dust, but absent in the local bedrock, are detectable in the soil. Similarly, the geochemistry and isotopic fingerprint of soil samples are more similar to dust than to local bedrock. End-member mixing models evaluating soil as a mixture of dust and rock suggest that the fine fractions of the sampled soils are dominated by dust deposition, with dust contents approaching 100%. Dust content is somewhat higher in soils over bedrock types more resistant to weathering. These results emphasize the dominant control that mineral dust deposition can exert on pedogenesis on the mountain critical zone.

1. Introduction

Soils are the foundation of high-mountain ecosystems. Knowledge of the factors that contribute to soil formation is, therefore, important to understanding the geoecology of mountain environments, particularly in a time of rapid climate change (Hagedorn et al., 2010; Singh et al., 2023; Tito et al., 2020). In the standard factorial model of soil formation (Jenny, 1983; Huggett, 1975), a key variable contributing to the properties of a soil is the nature of the soil parent material. Given their location on isolated topographic highs, alpine soils are systems in which the array of possible mineral parent materials can be simplified to two options: local bedrock, and mineral dust delivered by eolian processes (Derry and Chadwick, 2007). In periglacial mountain environments with low mean annual temperatures, rates of chemical weathering are reduced even though physical weathering through frost shattering may be enhanced (Dixon and Thorn, 2005). As a result, in settings where the local bedrock is relatively resistant to weathering, mineral dust deposition exerts a correspondingly larger influence on the accumulation of fine material and the enhancement of fertility that accompany soil formation (Arvin et al., 2017).

The southwestern United States is a significant dust emitter, due to its arid climate and sparse vegetative cover (Duniway et al., 2019). Dust derived from lowland landscapes is transported downwind toward mountain environments, where field

studies have evaluated the significance of dust deposition. For example, work in mountains surrounded by the Mojave Desert has illuminated the role of dust-influenced soils in regional biogeochemical cycling (Hirmas and Graham, 2011). In the San Juan Mountains of southwestern Colorado, comparison of dust and soil chemistry has demonstrated that dust is an important control on vegetation, soil, and surface water chemistry, and supported the conclusion that dust comprises as much of 40% of

35 the total mass of the mountain soils in this region (Lawrence et al., 2011, 2013). In central Colorado, mineralogical and geochemical analyses of mountain soils have further emphasized the importance of dust as a soil parent material (Muhs and Benedict, 2006; Litaor, 1987). Similarly, in northern Utah, soil profiles developed over siliciclastic bedrock were found to contain 50 to 80% dust, which has altered the physical properties of the soil and enhanced soil fertility through the addition of base cations (Munroe et al., 2020).

40 Collectively these studies, along with others from locations around the world (e.g. Peer et al., 2022; Küfmann, 2003; Greilinger and Kasper-Giebl, 2021; Johnston, 2001; Arvin et al., 2017), emphasize how dust deposition impacts the mountain critical zone (CZ), defined as the "dynamic interface between the solid Earth and its fluid envelopes" (Brantley et al., 2007) and underscore the importance of dust to soil development (Simonson, 1995). However, each of these projects focused on single localities, understandably constrained by the complexity inherent in documenting a ubiquitous process like dust

45 deposition across a broad region. This narrow spatial scope diminishes the utility of this prior work for supporting broader conclusions, obviates inferences about the role of dust deposition in different settings, and obscures the potential role of lithology as a regulator of the balance between local rock weathering and dust deposition in alpine pedogenesis. Accordingly, this project was designed to develop a comprehensive understanding of the effects of long-term dust deposition on pedogenesis in the mountain CZ across a range of lithologies in the southwestern United States.

50 2. Study Area

This research is centred on a network of six passive dust collectors (designated DUST-11 through DUST-16) deployed on mountain summits and high ridgelines with varying bedrock lithologies throughout the southwestern United States (Figure 1, Table 1). All sites display abundant geomorphic evidence of Pleistocene glaciation, however all but one of them are devoid of glaciers today (Osborn and Bevis, 2001). Dust collectors were intentionally positioned in windswept locations in alpine

55 settings above the Pleistocene glacier limit.

The easternmost collector, DUST-14, is located in the La Sal Mountains of eastern Utah, on the Colorado Plateau (Figures 1 and 2). The La Sals are comprised of three topographically distinct laccolithic masses of igneous rock that were intruded through sedimentary rocks during the Laramide Orogeny in the Oligocene (Hunt and Waters, 1958). Culminating with Mount Peale at 3877 m, the La Sals are the second highest mountain range in Utah. The DUST-14 collector is situated at an elevation

60 of 3669 m atop hornblende plagioclase trachyte (Ross et al., 1998) in a turf-covered saddle to the northeast of Manns Peak. The area around DUST-14 is simply denoted as "rubble land" on the USDA soils map.
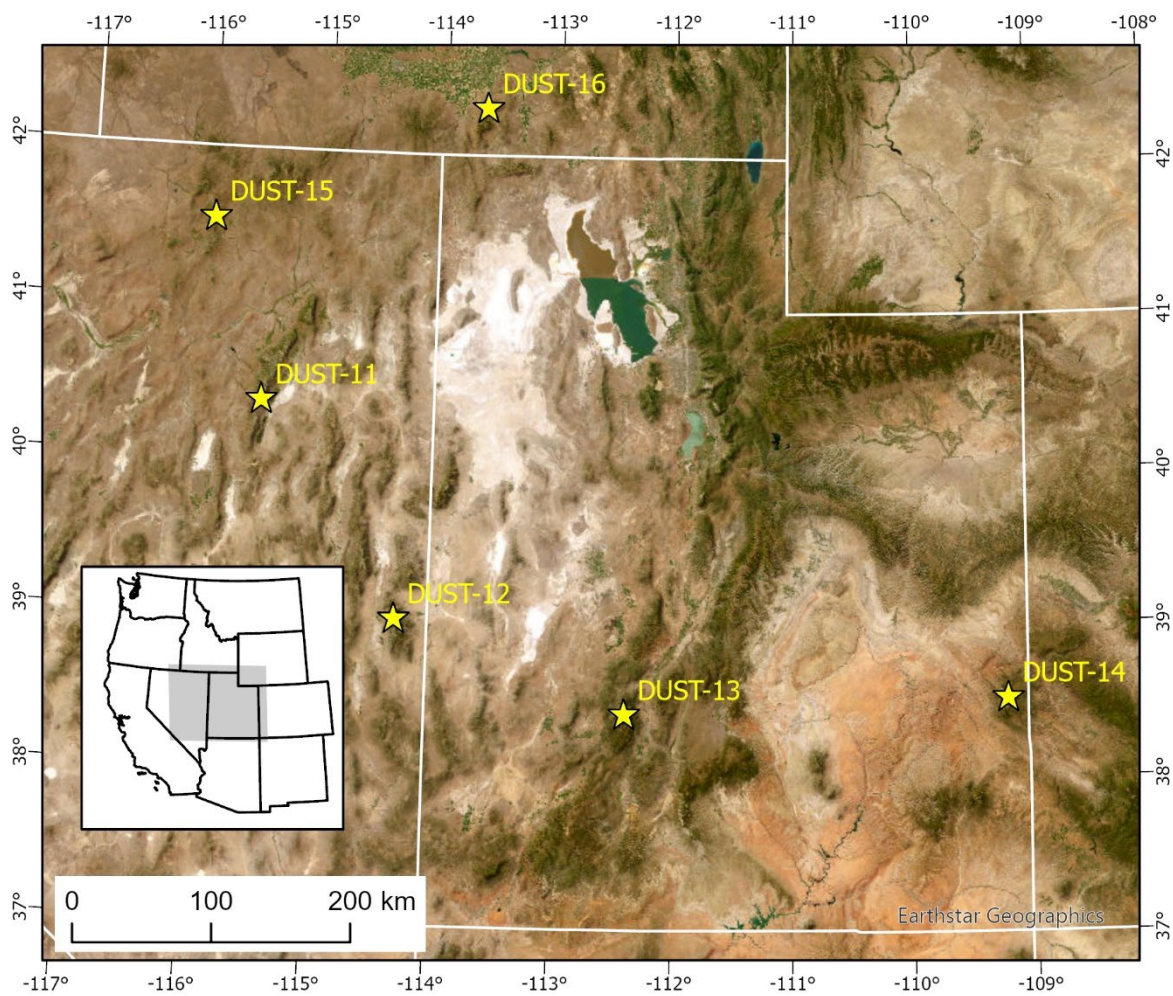
Figure 1. Map presenting the locations of the six passive dust samplers utilized in this study (yellow triangles). Background is a true-color satellite image from Earthstar Geographics. Inset shows the location of the main map (gray rectangle) in the western United States.

Table 1: Locations of Dust Collectors and Dates of Deployment				
Collector	Latitude d.ddddd	Longitude d.ddddd	Elevation m	Deployed m/d/yr
DUST-11	40.37586	-115.50140	2881	9/19/2020
DUST-12	38.99199	-114.31727	3684	9/21/2020
DUST-13	38.40102	-112.39293	3456	9/23/2020
DUST-14	38.51652	-109.21864	3669	9/24/2020
DUST-15	41.54140	-115.96658	3021	6/26/2021
DUST-16	42.31171	-113.65120	2785	7/4/2021
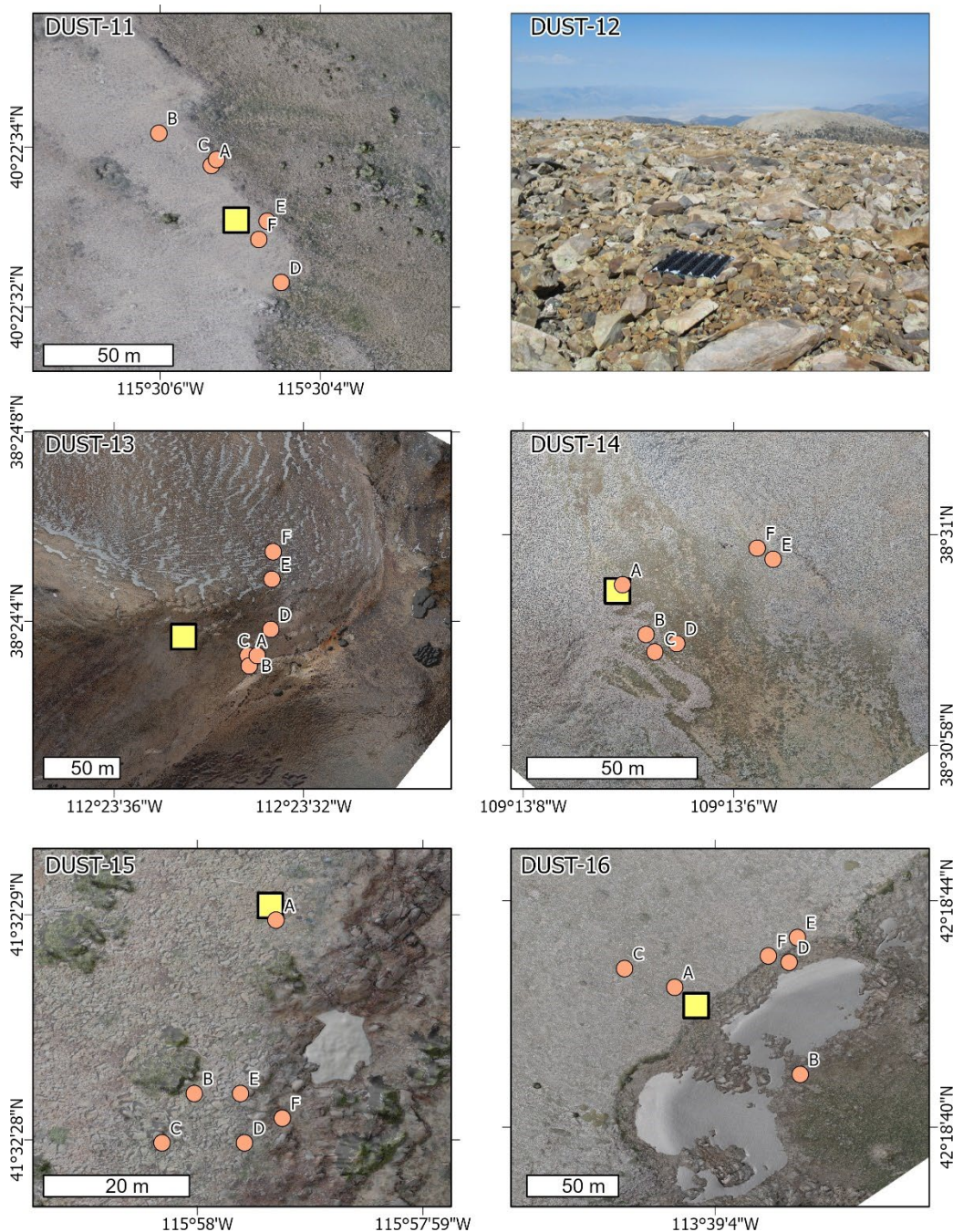
Figure 2. Site maps for the six study areas. For DUST-11, 13, 14, 15, and 16, the locations of the dust collector (yellow square) and soil samples (orange circles) are presented over a seamless orthophoto mosaic developed from pictures taken from an uncrewed aerial vehicle (UAV). For DUST-12, which is located in a national park where UAV operations are prohibited, the collector is shown in a ground-level photograph.

75   DUST-13 is located in the Tushar Mountains of southwestern Utah (Figures 1 and 2), the third highest mountain range in the state. The Tushars are the remnants of stratovolcanoes that formed between the Oligocene and the early Miocene (Steven, 1984). The highest mountain in the Tushars is Delano Peak at 3710 m. DUST-13 sits on bedrock mapped as trachyte at an elevation of 3456 m to the north of Bullion Pasture. Soils have not been officially mapped at DUST-13, and the landscape around the collector is nearly devoid of vegetation.

80   DUST-12 was deployed on the northeast shoulder of Wheeler Peak in the South Snake Range of eastern Nevada (Figures 1 and 2). Wheeler Peak, the centrepiece of Great Basin National Park, reaches an elevation of 4285 m, the second highest mountain in Nevada. DUST-12 is situated in a periglacial blockfield developed over quartzite bedrock (Hose and Blake Jr, 1976) at an elevation of 3684 m to the north of the main summit. The sole remaining glacier in the Great Basin is located ~200 m below and ~1 km to the southeast of the collector (Osborn and Bevis, 2001). At DUST-12, the soil is mapped as the

85   Wheelerpek series, a Lithic Cryothent. These soil profiles, which form over quartzite, only occur in the Snake Range of Nevada, where they cover ~1000 ha. Typical horizonation consists of a pair of A horizons with 10YR hues totalling 23 cm, over a thin C horizon resting on bedrock. Gravel content is high, subangular blocky structure is weakly developed, and mean annual soil temperature is from 1 to 4 °C.

       DUST-11 is positioned at the south end of the Ruby Mountains in eastern Nevada, 180 km northwest of DUST-12 (Figures

90   1 and 2). The Ruby Mountains are a metamorphic core complex of Paleozoic quartzites and carbonates, with granitic intrusions (Litherland and Klemperer, 2017). The protoliths of these rocks were emplaced during the Cambrian and Ordovician, followed by metamorphism and eventual uplift during the Neogene (Litherland and Klemperer, 2017). The Ruby Mountains reach elevations of 3470 m. DUST-11 is positioned at an elevation of 2881 m along a contact between quartzite and granitic bedrock on the sparsely vegetated southeastern shoulder of Green Mountain just outside the boundary of the federally protected Ruby

95   Mountain Wilderness. The area around the DUST-11 collector is mapped as the Lowemar series, a Xeric Humicryept in USDA soil taxonomy. These soil profiles are found in upland landscapes and form in residuum derived from metamorphic rocks. The typical pedon for the Lowemar contains multiple gravelly A horizons with 10YR hues totalling 50 cm in thickness over a C horizon of cobbly loamy fine sand.

       DUST-15 is located in the Independence Mountains of northern Nevada (Figures 1 and 2), which straddle the hydrologic

100   boundary between the Great Basin and the Snake River system. The area around the DUST-15 collector is dominated by Paleozoic quartzite bedrock, although a variety of Ordovician rocks including shales and cherts are present elsewhere in the range. The highest summit in the Independence Mountains is McAfee Peak at 3182 m. The DUST-15 collector sits at an elevation of 3021 on the narrow ridgeline extending northward from McAfee Peak. Tree clumps of stunted *Pinus flexilis* are presented in the vicinity of DUST-15 and the surrounding landscape is mapped as an association of rubble land with the

105   Longhike and Jarbidge soil series. These Haplocryoepts, which form in residuum derived from quartzite and rhyolite, cover 15,000 ha of mountain land in northern Nevada. The Jarbidge series, in particular, has a type locality on quartzite bedrock, making it the likely best match for the actual soils sampled at DUST-15. Jarbidge soil profiles feature a pair of light coloured (10YR 6/3) A horizons over a very pale brown Bw horizon resting on bedrock.

The DUST-16 collector was deployed in the Albion Mountains of southern Idaho (Figures 1 and 2). This range is part of
110 the Albion-Raft River-Grouse Creek metamorphic core complex, consisting of Precambrian granite, granitic gneiss, schist,
and amphibolite (Miller, 1980). The Albion Mountains reach elevations of 3150 m. DUST-16 is located at 2785 m on quartzite
bedrock at the southern edge of the gently sloping, partially vegetated upland summit of Mount Harrison. There is no official
soil map for the DUST-16 site.

3. Methods

115 **3.1 Field Methods**

3.1.1 Dust Collection

Each study site was equipped with an identical passive dust collector designed and constructed at Middlebury College (Munroe,
2022). These collectors are variations on the classic marble dust trap (Reheis and Kihl, 1995) altered for use in high-
precipitation mountain environments (Figure 3). Each is a 56x56-cm polycarbonate tray, composed of five, 7-cm deep troughs
120 with V-shaped cross-sections. Each trough is filled with ~400 black glass beads. These beads trap dust and retain it, while
heating in the sun to evaporate water, and leave concentrated dust at the bottom. The upper part of each trough has a row of
small drilled holes to allow for water drainage in times of excessive precipitation. Gasketed panels can be removed from the
end of each trough to facilitate dust removal. The collectors are positioned on a relatively flat surface and held down on the
edges by rocks. Each is also equipped with an automated temperature data logger to constrain the duration of winter snow
125 cover. Full technical designs for the collectors have been previously published (Munroe, 2022).

Dust is removed from a collector by washing with distilled water. The beads are removed with a slotted spoon, transferred
to a colander, and rinsed into an acid-washed 1L Nalgene bottle. After the beads are removed, each trough is rinsed with
additional water and the collector is scrubbed with a small brush. The process yields 5 L of water with suspended dust that is
shipped back to the laboratory for analysis.

130 Collectors DUST-11 through DUST-14 were deployed in the fall of 2020 (Table 1). DUST-15 and DUST-16 were added
in July, 2021, at the same time that DUST-11 through DUST-13 were emptied. All collectors were emptied again in the fall
of 2021 (an annual sample for DUST-14 and summer samples for the others), in July 2022 (winter dust samples), and in
October, 2022 (summer dust samples). This approach yielded a total of 22 dust samples.

3.1.2 Soil and Rock Collection

135 In July, 2022, soil and rock samples were collected in the general proximity of their corresponding dust collector. At DUST-
12, five samples (A-E) were collected, and at the other sites, six samples (A-F) were gathered (Figure 2). Sampling involved
canvassing the area around each collector to identify locations where it was possible to collect a representative soil sample
with a hand shovel. Each sample was collected in a new quart-size Ziploc bag, and the sampling position was recorded with

140

Figure 3. Close-up photograph of the DUST-12 collector showing the sampler design (5 troughs with V-shaped cross sections filled with black, glass marbles), and the typical ground-level deployment. In the background a dust storm lifting material from the ground surface in the Spring Valley and transporting it to the east (right) into the North Snake Range is obvious.

145 a handheld GPS. Because exposures of local bedrock are rare in the periglacial landscapes surrounding each collector, pebbles contained within each soil samples were considered to represent the underlying bedrock. This assumption is considered acceptable given the presumably slow rates of chemical weathering in these cold, high-elevation environments.

3.2 Laboratory Methods

3.2.1 Dust Samples and Grain Size Analysis

150 All of the samples (water bottles from 22 dust collections and 35 bags of mixed soil and rock) were shipped back to Middlebury College for analysis. In the laboratory, soil and rock were separated for each sample using a 2-mm sieve. Material passing through the sieve was considered soil (equivalent to the "fine earth fraction"), while larger fragments that did not pass were considered to represent the local bedrock. Plant roots and other organic materials was picked out and discarded along with any lichens scraped from the rock fragments. The <2-mm soil samples were transferred to new Ziplock bags. The rocks sieved

155 from each sample were processed in a jaw crusher, and converted to a fine powder in a Shatterbox. This process generated 35 soil and 35 samples of powdered rock.

The grain size distribution of the soil samples was determined with laser scattering in a Horiba LA-950 analyser. Approximately 5 cm^3 of each sample was removed and reacted with 35% H_2O_2 at room temperature for 7-10 days to remove organic matter. After the reaction had subsided, samples were centrifuged and rinsed with distilled water. Sodium

160 hexametaphosphate (3%) was added as a dispersant and all samples were physically mixed and sonified prior to analysis. The LA-950 has an effective range from 10 nm to 3 mm, and a standard refractive index of 1.54 with an imaginary component of 0.1i was used in the calculating the grain size distribution of each sample on a volume basis.

To isolate the fine fraction from the soil samples most closely matching the grain size distribution of the dust, a representative portion of each soil sample was thoroughly mixed with distilled water in a 1000-mL graduated cylinder. After

165 settling for 2 minutes, a vacuum flask was used to collect the top 200 mL of water and suspended soil. This subsample was then freeze dried. Once fully desiccated, these samples were gently ground by hand using a mortar and pestle before being ignited at 1000 °C for 30 minutes in a Leco TGA-701 thermogravimetric analyser to determine percent loss on ignition (LOI).

Dust samples were concentrated from the 5 L of water from each collector by centrifuging at 6000 rpm, with repetitive decanting. Organic matter was eliminated by treatment with 35% H_2O_2 over 7 days. After this step, samples were wet-sieved

170 to 63 µm. Particles >63 µm were considered likely of local origin, most likely to represent exotic mineral dust. Both fractions were dried and weighed to calculate depositional fluxes, and the <63-µm fine dust fraction was retained for further analyses.

3.2.2 Soil Analysis

Roughly 150 cm^3 of each homogenized soil sample was removed and sent to the Agricultural and Environmental Testing Laboratory at the University of Vermont. Soil pH was measured at a 1:2 in 0.01M $CaCl_2$ and converted to water equivalent.

175 Organic matter was measured by loss on ignition at 375 °C and converted to Walkley-Black organic matter equivalent. Morgan

solution (pH 4.8 ammonium acetate) was used to extract soil nutrients at a 1:5 ratio for 15 minutes. P was analysed through colorimetric flow injection. Other nutrients were measured by ICP-OES.

3.2.3 Mineralogical Analyses

All samples of soil, rock, and dust were examined for their mineralogical composition at Middlebury College using a Bruker
180   D2 Phaser X-Ray Diffractometer (XRD) with a copper K-alpha radiation source and a Lynleye XE-T solid state detector. As an initial check for consistency, soil samples A through C for each site were analysed from 3 to 40° 2Θ through a 7-minute scan. After confirming mineralogical homogeneity, a composite sample was created for each site by combining equal amounts of each soil sample. This process generated a ~6 g composite sample for collector (the composite sample for DUST-12 weighed 5 g). This approach was replicated with the rock samples to produce similar composite samples representative of the
185   rock at each site.

Composite samples of rock and soil, as well as the dust samples, were scanned from 3 to 40° 2Θ continually for 13-minutes at 30 kV and 10 mA. Dust samples were wetted and mixed, and transferred to a glass slide with an eye dropper before analysis; soil and rock powders were analysed as random powders. XRD results were analysed semi-quantitatively by measuring the area under the curve of diagnostic peaks for quartz (20.8 and 26.7° 2Θ) and feldspar (22.0 and 22.7° 2Θ). A
190   mineralogical index (Feld/Qtz) for each sample was then calculated as the quotient of the sum of the area beneath the two feldspar peaks and the sum of the area beneath the two quartz peaks.

3.2.4 Geochemical Analyses

Abundances of 50 major and trace elements were in the rock, soil, and dust samples were determined by Inductively Coupled Plasma Mass Spectrometry (ICP-MS) at the University of Utah ICP-MS Metals and Strontium Isotope Facility. Dust samples
195   from 2020 through 2021 were run in March, 2022. Dust samples from 2021 through 2022 were run in January, 2023. Rock and soil samples were run in May, 2023. Each analysis run included standard reference material (SRM) 1643f, 4 multiple chemical blanks, and four aliquots of standard AGV-1. All samples were dissolved in HF before analysis, therefore concentrations of Si were not measured. Recoveries for individual elements relative to the AGV-1 standard (Jochum et al., 2016) averaged 105% (dust 2020-21), 98% (dust 2021-22), and 97% (rock and soil).
200   Strontium and neodymium isotope analysis was conducted in the Department of Geoscience at the University of Wisconsin-Madison using thermal ionization mass spectrometry (TIMS) and multi-collector inductively coupled plasma-mass spectrometry (MC-ICP-MS). A total of 14 dust samples was analysed during two analytical sessions in spring 2022 and winter 2023. Three were from winter 2020-21, four were from summer 2021, one (DUST-14) was an annual sample from fall 2020 through fall 2021, and six were composite samples created from mixtures of winter 2021-22 and summer 2022 dust weighted
205   by the relative contributions of each of those seasons to the total annual mass. Composite samples of soil and rock from each of the six sites were also analysed. Sample dissolution and column chemistry procedures were performed following the details

presented in Munroe et al. (2020). Total procedural blanks ranged from 35-60 pg Sr and 93-225 pg for Nd. These blanks are insignificant (minimum sample to blank ratio of 1800) and no blank corrections were applied.

210 Strontium samples were analysed using a Micromass Sector 54 TIMS. Samples analysed in spring 2022 were loaded onto Ta filaments with 1M H_3PO_4. Samples analysed in winter 2023 had lower Sr abundances, so they were loaded onto Re filaments with TaF activator and 1M H_3PO_4. All samples were analysed using a three-jump multi-collector dynamic analysis with exponential normalization to an $^{87}Sr/^{86}Sr = 0.1194$ at a $\sim 3\times 10^{-11}$ A $^{88}Sr^+$ ion signal. Errors (2-σ) reported for individual analyses are based on the in-run statistics and are reported as 2 standard errors (2-SE) of the mean, based on the 120 ratios collected during the dynamic analysis.

215 Neodymium samples were analysed using a Nu Instruments NP2 MC-ICP-MS with enhanced sensitivity interface for samples diluted to a concentration of 50 ppb Nd in 2% HNO_3. A Cetac Aridus II fitted with a Savillex 50 µl min^{-1} concentric flow nebulizer was used to aspirate the sample into the instrument; this produced a typical $^{144}Nd^+$ ion signal of $\sim 5\times 10^{-11}$ A. Neodymium isotope ratio measurement used static multi-collector analysis routine consisting of collecting 40 ratios (10s of integrations) with an initial on-peak-zero subtraction based on a one-minute analysis of the 2% HNO_3 blank acid conducted
220 before the Nd isotope analysis. Instrumental mass bias was corrected by exponential normalization to a $^{146}Nd/^{144}Nd = 0.7219$. Every third sample was a bracketing standard consisting of the internal UW Ames II Nd isotope standard. A correction factor for the exponentially normalized Nd isotope ratios was calculated based on taking the ratio of the measured exponentially normalized Nd isotope ratios and the long-term Nd TIMS isotope ratio analysis of Ames II Nd for all Nd ratios. This correction factor was applied to samples and standards run as unknowns. The $^{143}Nd/^{144}Nd$ ratio and errors reported for the Nd isotope
225 analyses are the average and 2 standard deviation based on two replicate analyses. Values of ε_{Nd} were calculated using a $^{143}Nd/^{144}Nd$ of 0.512634 for modern CHUR.

During the course of this study, the average $^{87}Sr/^{86}Sr$ ratio for the NIST SRM-987 Sr standard was 0.710267 ± 0.000015 (2σ; n=15) for Ta filaments and 0.710269 ± 0.000016 (2σ; n=25) for Re filaments. The USGS EN-1 standard yielded an average $^{87}Sr/^{86}Sr$ ratio of 0.709199 ± 0.000007 (2σ; n=4) on Ta filaments and 0.709196 ± 0.000018 (2σ; n=16) on Re filaments.
230 For each filament type both standards yield values consistent with the long-term averages for the lab. For Nd, external reference material JNdi and in-house standard Ames I Nd were analysed along with samples and yield average $^{143}Nd/^{144}Nd$ values of 0.512112 ± 0.000017 (2σ; n=8) and 0.512143 ± 0.000010 (2σ; n=9), respectively; which are also consistent with the lab long-term measurement averages of these standards.

3.2.5 Data Reduction and Statistics

235 Data were organized in MS Excel, analysed in SPSS 28.1, and plotted using Grapher 19.4. Results from XRD analysis were viewed and compared in Eva 6.1 software. Summary statistics for geochemical results were calculated for each element quantified, for each site, and for each type of sample (dust, soil, rock). To reduce the complexity of the overall geochemical dataset, elemental abundances were normalized to Fe (Reheis et al., 2002; Munroe et al., 2020) and converted to log10 before a principal component analysis was conducted using a varimax rotation with all elements (n=50). A second principal

240 component analysis was conducted using a subset of elements (also normalized to Fe and converted to log10) previously demonstrated to not have been impacted by anthropogenic activity post European settlement (Reynolds et al., 2010). Non-parametric statistics were utilized to compare means between sample sites (Kruskal-Wallis test) and in evaluating correlations (Spearman rank correlation), given the generally small number of samples of each type.

Starting from the logic that these soil samples are a mixture of dust and rock end members (Crouvi et al., 2013), dust
245 fractions (*fDust*) within each soil sample were calculated from the ratio (δ) of immobile trace elements Cr/Ta (Reynolds et al., 2010) and from the ratio Feldspar/Quartz (Litaor, 1987) in the soil, dust, and rock using a two-end member mixing equation following previous studies (Lawrence et al., 2011; Capo et al., 1998; Graustein and Armstrong, 1983):

$$fDust = \frac{[\delta_{Soil} - \delta_{Rock}]}{[\delta_{Dust} - \delta_{Rock}]}$$

250 The value of *fDust* was also estimated from the $^{87}Sr/^{86}Sr$ ratio and from ε_{Nd} using a concentration-weighted mixing model (Colville et al., 2011; Faure, 1997; Munroe et al., 2020):

$$R_m = \frac{f_{Dust}[C_e](R_{Dust}) + f_{Rock}[C_e](R_{Rock})}{f_{Dust}[C_e] + f_{Rock}[C_e]}$$

255 where R_m is the value of $^{87}Sr/^{86}Sr$ or ε_{Nd} for a particular sample. C_e is the average concentration of Sr or Nd measured in the dust and rock end members. R is the concentration-weighted average value of $^{87}Sr/^{86}Sr$ or ε_{Nd} in the rock and dust end members. The sum of *fDust* and *fRock* equals 1, therefore *fRock* = (1- *fDust*).

Mixing models were constructed with $^{87}Sr/^{86}Sr$ and ε_{Nd} in average dust and rock end members, and *fDust* was determined for the mean $^{87}Sr/^{86}Sr$ or ε_{Nd} in each soil sample, as well as ± one standard error. To visualize the potential error envelope of
260 these estimations, the mixing models were also constructed with each of the individual dust samples (three at DUST-11, 12, and 13, two at DUST-14, 15, and 16). Finally, the ensemble of estimates of *fDust* obtained by different approaches was averaged to produce an overall *fDust* estimate for each site.

4. Results

4.1 Soil Properties

265 The soils at the six dust collectors are uniformly coarse, cold, and poorly developed, consistent with their locations in high mountain environments. At DUST-11, 12, and 15, the sampled soils closely match the series mapped for these locations. At DUST-13, 14, and 16, where soil maps are not available, soil profiles resemble those at the other sites, with gravelly 10YR A horizons and a shallow depth to bedrock. At DUST-11, 15, and 16 mostly bare fine soil was present directly at the ground surface with only sparse vegetation. In contrast, at DUST-12, fine soil was concentrated in vegetated islands generally <2-m

270 in diameter surrounded by blockfields of broken quartzite with open void space. At DUST-13, fine soil was present beneath a concentration of cobble-gravel and was rarely exposed at the surface. At DUST-14, the soil surface was vegetated with continuous tundra vegetation.

In contrast to their visual similarity, soils at the six dust collector sites vary considerably in their grain size distribution (Table 2). The samples from DUST-14 exhibit the coarsest mean grain size (118 um) whereas the mean at DUST-12 is the

275 finest (32 um). Soils at DUST-11, 15, and 16 all have a mean grain size of ~40 um. Sand content is highest at DUST-14 (39%) and lowest at DUST-12 and 15 (14%). Silt content ranges from 55% (DUST-14) to 77% (DUST-12), and the abundance of clay-size material (<2 um) ranges from 6% (DUST-14) to 13% (DUST-13). Nearly all of the soil samples have textures of Silt Loam (Figure 4), although one sample from DUST-14 is a Sandy Loam, and one from DUST-15 classifies as Silt.

Considerable chemical variation also exists between the soils (Table 2, Figure 5). Soils at DUST-11 and 12 have the

280 highest pH values (averaging 7), whereas DUST-15 soils are most acidic (mean pH of 6). Organic matter content is much higher at DUST-15 (mean of 12%) than at the other sites (2-6%). Extractable P, K, Ca, Mg, S, and Mn are highest at DUST-12; the lowest values for extractable P and K are at DUST-14, and the lowest extractable Ca, Mg, S, and Mn are at DUST-13. Exchangeable acidity is highest at DUST-15, and overall cation exchange capacity is highest at DUST-12.

4.2 Mineralogy

285 X-ray diffraction successfully detected a range of mineral phases in the dust, soil and rock samples including quartz, feldspars, mica, kaolinite, smectite, and illite (Figure 6). Dust samples routinely contain all of these minerals, aside from smectite, which was only present in one collection from DUST-14. In contrast, the rock samples at DUST-11, 12, 15, and 16, reveal a nearly pure quartz composition, consistent with the quartzite bedrock mapped for these locations. At DUST-13 and 14, which are located over volcanic bedrock (trachyte), the rock sample exhibits XRD peaks for feldspar in addition to quartz.

290 Significantly, at all sites, soil samples contain minerals not present in the underlying rock. For example, feldspars are present in the soil at DUST-11, 12, 15 and 16, despite their absence in the bedrock. Illite is present in the soil at DUST-11, 13, 15, and 16; kaolinite is detectable in the soil at DUST-11, 13, and 15. On the other hand, the smectite detected in the first dust sample from DUST-14 (fall 2020 to fall 2021) is not present in the composite soil sample from this site.

Measuring the area under the curve of diagnostic peaks for quartz and feldspar provided a semi-quantitative approach to

295 evaluating the XRD results (Table 3). At all sites except DUST-14, values of Feld/Quartz are lowest in bedrock (~0.04); at DUST-14 the ratio is elevated (2.46) by the large amounts of feldspar in the trachyte. Values are intermediate in all soil samples (~0.5), and highest in dust (~0.9).

Table 2. Summary of Soil Grain Size and Fertility Data								
Sample	**Units**	**All**	**DUST-11**	**DUST-12**	**DUST-13**	**DUST-14**	**DUST-15**	**DUST-16**
pH	--	6.5	7.0	7.1	6.5	6.3	6.0	6.2
OM	%	6.0	4.1	4.9	2.4	6.3	11.9	6.1
ext. P	ppm	4.5	3.9	11.4	1.4	1.3	5.8	4.5
ext. K	cmol(+)/kg	0.9	1.2	1.4	0.5	0.2	0.9	1.3
ext. Ca	cmol(+)/kg	11.2	12.7	13.2	8.3	12.2	10.8	10.5
ext. Mg	cmol(+)/kg	2.9	3.4	5.5	1.8	2.1	2.4	2.5
ext. S	ppm	5.7	7.8	8.6	3.7	5.0	4.0	5.8
ext. Mn	ppm	5.3	7.1	4.1	2.6	2.6	5.8	9.4
ext. B	ppm	0.7	1.1	1.1	0.3	0.4	0.5	0.8
ext. Cu	ppm	0.1	0.1	0.1	0.1	0.1	0.2	0.1
ext. Zn	ppm	0.6	0.3	0.3	0.3	0.2	1.8	0.4
ext. Na	ppm	18.1	40.5	19.6	13.0	12.7	11.7	11.3
ext. Al	ppm	34.1	14.2	13.0	20.0	46.3	64.0	43.7
Exch_Acid	cmol(+)/kg	1.6	0.2	0.1	1.0	2.4	3.9	1.9
CEC	cmol(+)/kg	16.6	17.5	20.2	11.6	16.9	17.9	16.2
Ca_Base_Sat	%	67.5	72.8	65.5	71.2	72.7	59.4	63.4
K_Base_Sat	%	5.3	6.9	6.9	4.6	1.1	4.9	7.3
Mg_Base_Sat	%	16.7	19.0	27.0	15.4	12.4	13.0	15.0
Mean	μm	56.6	39.9	31.6	63.9	117.8	41.8	40.4
Median	μm	20.9	16.5	17.2	16.4	40.5	14.1	20.3
Mode	μm	25.3	20.0	17.6	14.7	54.4	15.1	28.6
Std. Dev.	μm	85.4	56.3	40.1	107.4	176.6	71.5	53.1
Coarse Sand	%	1.7	0.0	0.0	2.3	5.8	1.6	0.0
Med Sand	%	3.2	1.5	0.3	4.9	10.1	0.7	1.2
Fine Sand	%	6.4	7.4	3.7	7.1	9.8	3.0	6.8
Very Fine Sand	%	10.3	10.8	10.2	7.8	13.3	8.2	11.6
Coarse Silt	%	16.5	15.5	19.3	12.6	16.9	16.6	18.8
Medium Silt	%	18.8	17.4	22.4	18.1	15.4	19.2	20.7
Fine Silt	%	15.4	16.4	16.9	15.8	10.6	17.4	15.5
Very Fine Silt	%	18.1	21.0	18.3	18.9	11.7	22.2	16.4
Clay	%	5.5	6.1	5.8	5.6	4.2	6.6	4.7
Colloid	%	4.2	3.9	3.1	7.0	2.1	4.5	4.4
<2um	%	9.7	10.0	8.8	12.6	6.3	11.2	9.1
%Sand	%	21.6	19.7	14.2	22.1	39.1	13.5	19.6
%Silt	%	68.8	70.3	76.9	65.3	54.6	75.4	71.3
%Clay	%	9.7	10.0	8.8	12.6	6.3	11.2	9.1
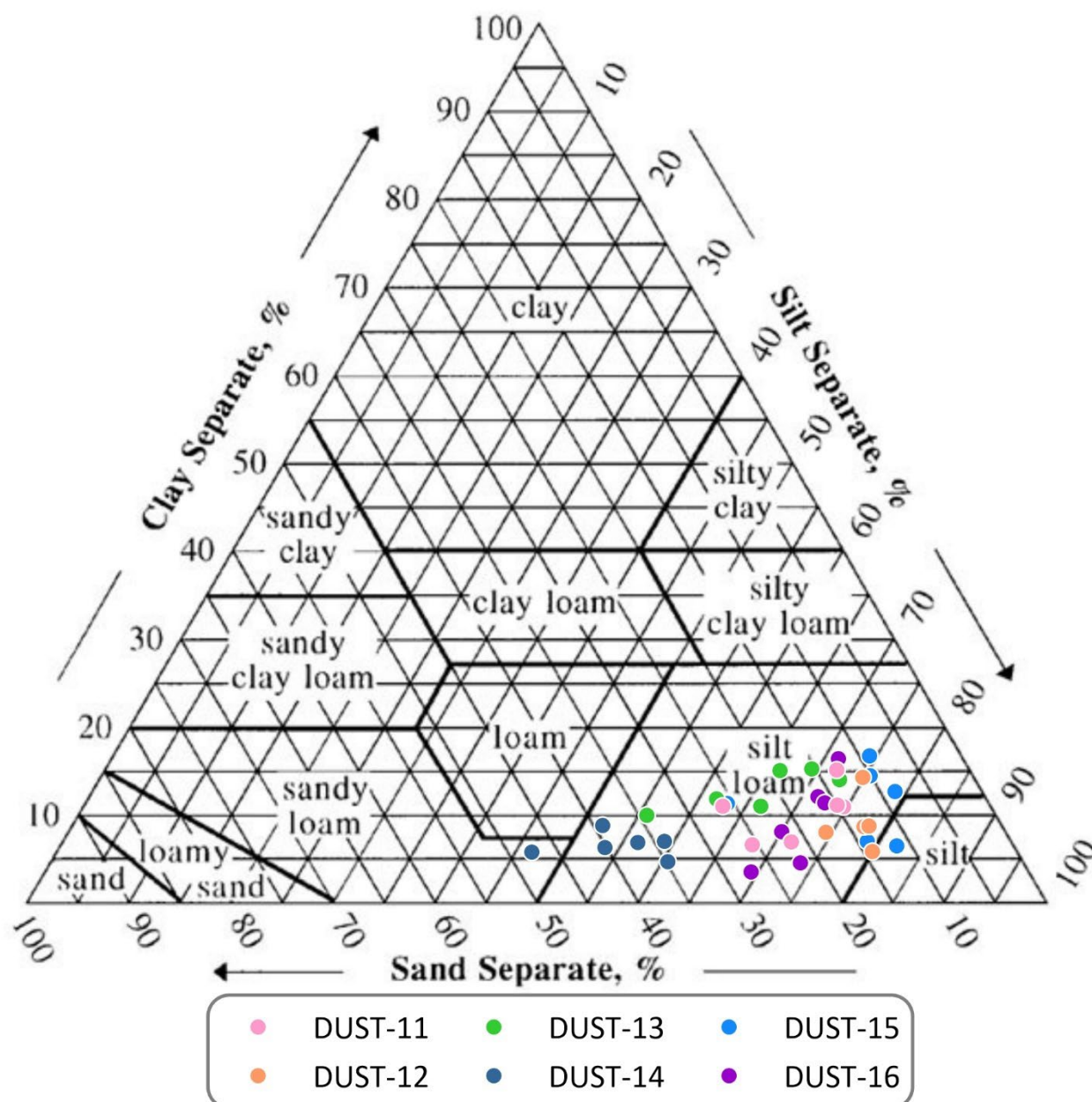
Figure 4. Standard US Department of Agriculture ternary diagram presenting soil textures measurements at the six study sites. Nearly all samples fall in the Silt Loam texture class, with one sample from DUST-15 classifying as Silt, and one from DUST-14 as Sandy Loam.
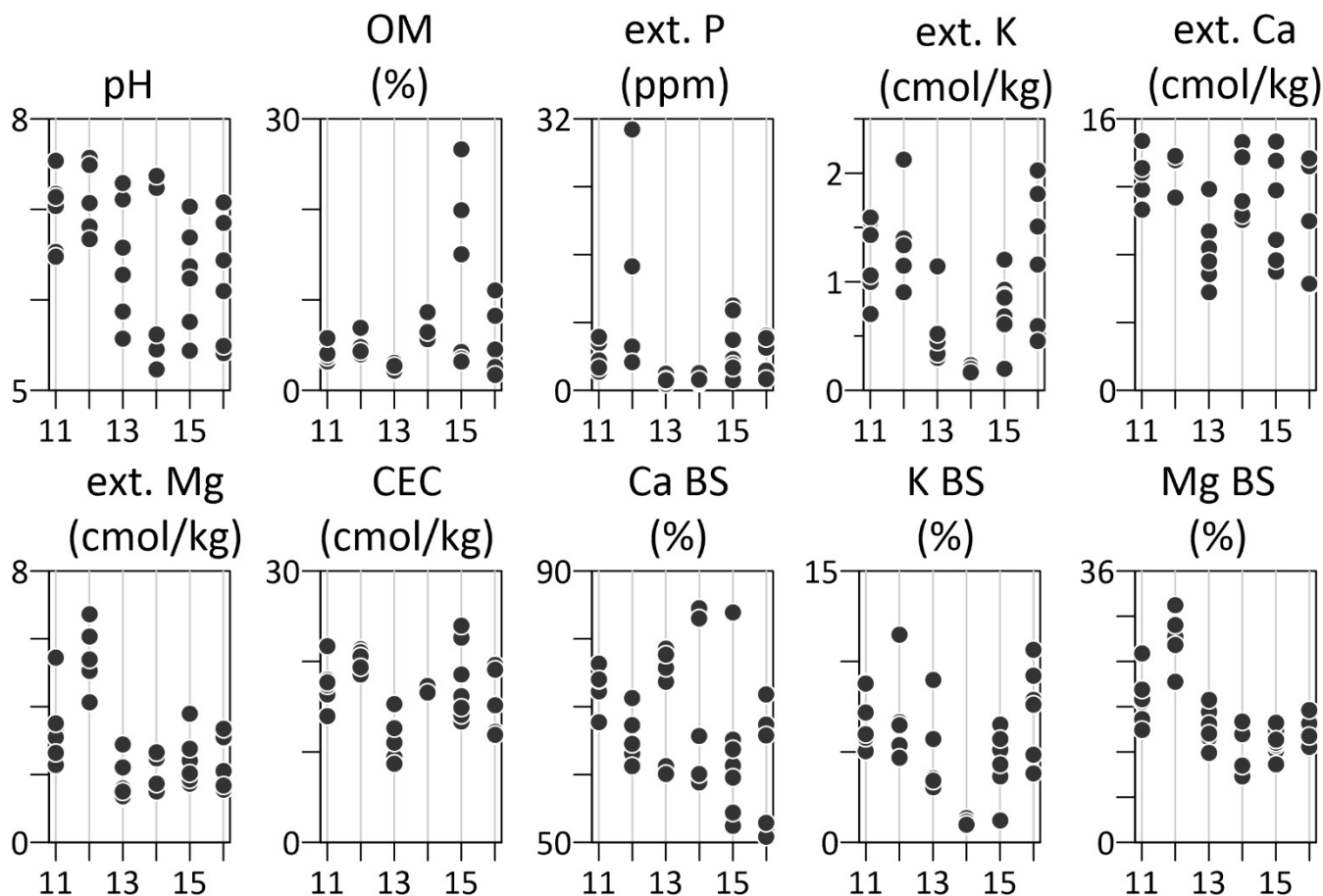
Figure 5. Summary of soil fertility measurements made at each of the study sites. The X-axis of each plot presents collectors 11 through 16. "OM" is organic matter. "ext." indicates extractable. "CEC" is cation exchange capacity. "BS" is base saturation.

305
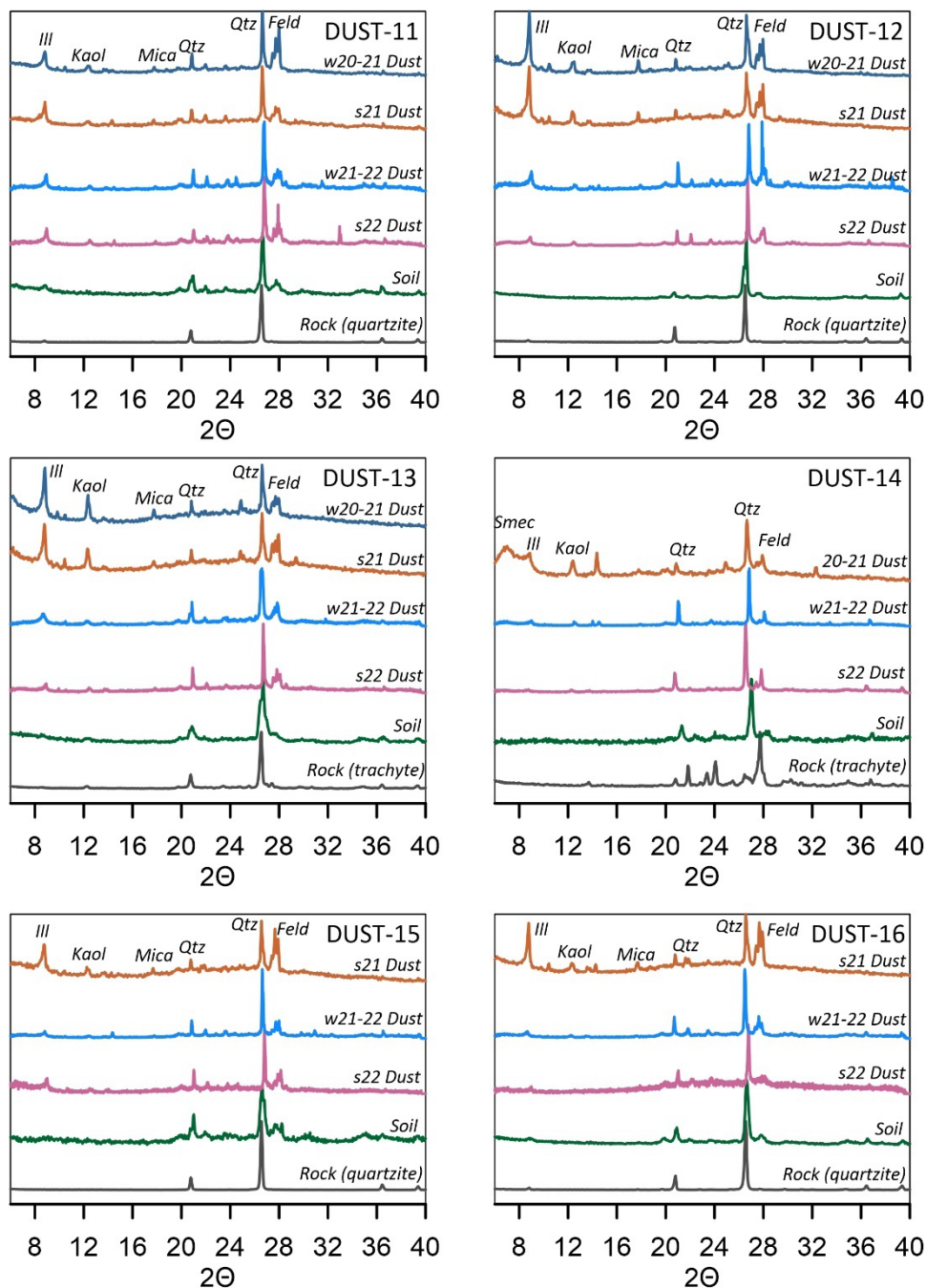
Figure 6. X-ray diffraction (XRD) results for samples of dust, soil, and rock at the six study sites. Individual dust samples are presented to emphasize the general seasonal and interannual consistency of dust composition. "w20-21" is dust accumulating during the winter of 2020-21. "s21" is dust from summer 2021. "w21-22" is dust from the winter of 2021-22. "s22" is dust from summer 2022. Soil and rock samples are a composite of the individual samples collected at each site. Prominent mineral peaks are identified: "Ill" is illite, "Kaol" is kaolinite, "Mica" indicates K-mica, "Qtz" is quartz, and "Feld" is Ca and Na feldspar.

Table 3. X-ray Diffraction Results					
Collector	Sample*	Qtz 4.26 Å	Qtz 3.34 Å	Feld 4.02 Å	Feld 3.25 Å	∑Feld/∑Quartz
11	w20-21 Dust	7.67	31.26	7.68	40.48	1.24
11	s21 Dust	7.48	26.82	7.68	22.36	0.88
11	w21-22 Dust	0.78	3.83	0.64	2.95	0.78
11	s22 Dust	0.80	4.19	0.46	3.19	0.73
11	Soil	12.47	28.41	4.90	16.40	0.52
11	Rock	24.11	115.83	0.00	3.70	0.03
12	w20-21 Dust	8.32	39.73	5.08	33.69	0.81
12	s21 Dust	4.30	25.27	4.80	27.89	1.11
12	w21-22 Dust	0.86	3.56	0.45	3.55	0.90
12	s22 Dust	1.13	6.20	0.82	4.06	0.67
12	Soil	6.28	42.22	5.74	16.50	0.46
12	Rock	25.70	101.73	0.00	3.80	0.03
13	w20-21 Dust	9.2	24.52	4.7	21.15	0.77
13	s21 Dust	5.59	27.97	3.87	26.77	0.91
13	w21-22 Dust	2.36	6.60	0.51	3.48	0.44
13	s22 Dust	1.63	4.70	0.65	3.86	0.71
13	Soil	9.65	30.80	3.76	8.50	0.30
13	Rock	17.70	73.27	2.27	7.30	0.11
14	20-21 Dust	8.39	29.17	4.26	21.21	0.68
14	w21-22 Dust	1.32	3.30	0.00	1.49	0.32
14	s22 Dust	0.69	2.79	0.00	0.42	0.12
14	Soil	2.50	7.00	1.74	4.63	0.67
14	Rock	8.41	19.85	13.74	55.89	2.46
15	s21 Dust	9.06	24.49	9.87	32.06	1.25
15	w21-22 Dust	1.05	4.83	0.66	3.42	0.69
15	s22 Dust	0.37	1.26	0.26	0.95	0.74
15	Soil	7.93	18.49	5.67	13.58	0.73
15	Rock	24.10	132.61	0.00	3.00	0.02
16	s21 Dust	10.13	23.01	7.03	19.67	0.81
16	w21-22 Dust	1.42	6.67	0.85	4.00	0.60
16	s22 Dust	0.48	1.93	0.21	0.62	0.34
16	Soil	12.97	37.91	5.60	14.70	0.40
16	Rock	25.03	126.45	0.00	2.77	0.02
*"w" designates winter dust, "s" designates summer dust					

315

4.3 Geochemistry

ICP-MS analysis provided a comprehensive perspective on the geochemistry of each sample. The elements Na, Mg, Ca, P, Cr, Cu, Zn, Ni, Sr, Zr, Mo, Cd, Sn, Sb, Ba, Pb, and Bi have the highest average abundances in dust samples (Tables S1-S3). Be, Al, K, Sc, Mn, V, Fe, Ti, Ga, Rb, Y, As, Nb, Hf, Ta, Tl, Th, U, and the rare earth elements are most abundant in soils.
320   Only Co and W are most abundant in bedrock samples, which are likely dominated by Si, which was not measured. The high W abundance likely reflects the W-bearing puck utilized in the shatterbox. Overall, the most abundant element measured is Al (max of 10.2% in dust, 12.3% in soil, and 9.3% in rock). The first two principal components determined with a varimax rotation (Kaiser-Meyer-Olkin score of 0.857) for the full dataset after normalizing to Fe and a log10 transformation explain 67% of the variance. The first component (PC-1) is dominated by REEs, Th, Zr, U, Rb, K, and Al. The second component
325   (PC-2) contains metals like Sb, Cu, Cd, and Zn. Values of PC-1 and PC-2 for dust, soil, and rock are distinct from one another at each site; at sites 11, 12, 15, and 16 most of the variability is in PC-2.

As noted in previous studies, many trace elements in modern mineral dust are present at abundances greatly in excess of their crustal averages, suggesting an anthropogenic contribution from mining (Munroe, 2014; Lawrence et al., 2013, 2011; Reheis et al., 2002). This situation presents a challenge for the present study, which assumes that modern dust is representative
330   of the long-term average dust that has contributed to soil formation. A solution is to identify elements in the dust are least likely to be enriched by anthropogenic activity. Toward this end, a study of lacustrine sediment records from northern Utah identified that Al, Ca, Sc, Ta, U, Th, Ti, Zr, Cr, Rb, K, Na, and Nb did not increase in abundance in concert with the European settlement and the start of widespread mining and smelting in this region (Reynolds et al., 2010). Of these, Ca, Zr, Cr, and Na are generally most abundant in the dust samples reported here, and Al, Sc, Ta, U, Th, Ti, K, Rb, and Nb are most abundant in
335   soil. Principal component analysis (Kaiser-Meyer-Olkin score of 0.775) of the abundances of these elements ratioed to Fe and converted to log10 places Th, Nb, Rb, Al, K, U, Ta, and Zr on component 1, which explains 55% of the variance. Na and Ca are associated with component 2 (18%), whereas Cr, Ti, and Sc are associated with PC-3 (11%). Samples of dust and soil overlap strongly in a bi-plot of PC-1 vs. PC-2 and exhibit strong dissimilarity with rock samples (Figure 7).

Rare earth elements (REEs) provide another approach for comparing material from the different study sites (Zheng et al.,
340   2021). In particular, the ratio La_n/Lu_n where the subscript "n" designates values normalized to a chondrite standard (Nakamura, 1974), capture the difference in abundance between light REEs (La) and heavy REEs (Lu). Similarly, calculation of Eu*, the Eu anomaly, is useful for assessing the geologic history of individual samples (e.g. Pourmand et al., 2014; Tang et al., 2013). Overall average values of La_n/Lu_n range from 8.48 at DUST-15, to 12.5 at DUST-16 and vary significantly between sites (Kruskal-Wallis H of 24.534, P<0.001). Values of Eu* are all <1, indicating Eu depletion, and are lowest at DUST-13, with
345   a mean of 0.35. The highest mean Eu* value of 0.87 is at DUST-14. Once again, values are significantly different between sites (Kruskal-Wallis H of 59.397, P<0.001). Plotting La_n/Lu_n vs. Eu* at the six sites reveals a great deal of similarity between dust and soil at all locations and emphasizes the distinctions between the rock samples (Figure 8).
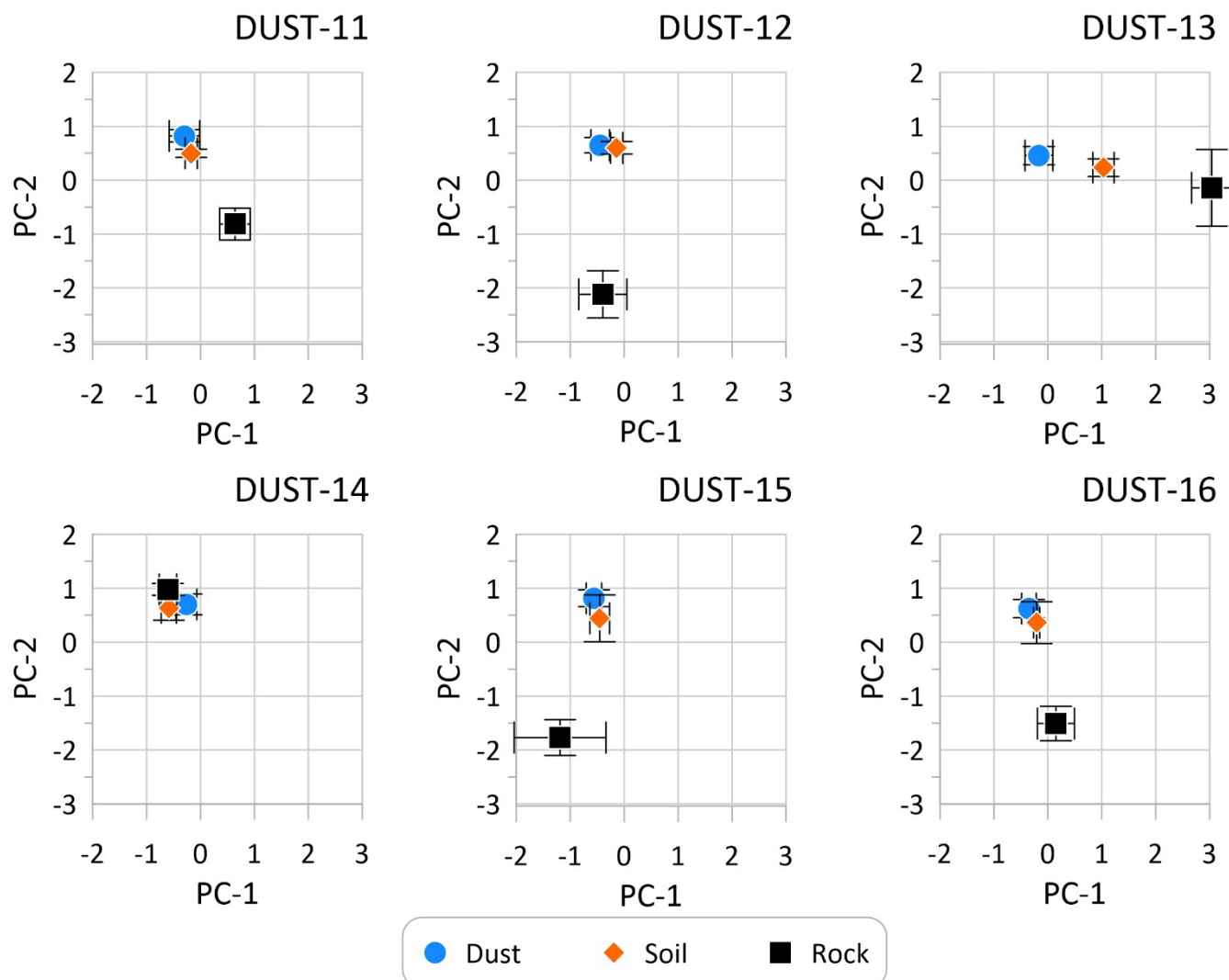
Figure 7. Results of principal component analysis for 13 elements quantified in the dust, soil, and rock samples that were previously
350 **demonstrated not to have been impacted by human activity following European settlement (Reynolds et al., 2010). Values of the first principal component (PC-1) and second principal component (PC-2) are plotted as mean ± 1 standard deviation.**
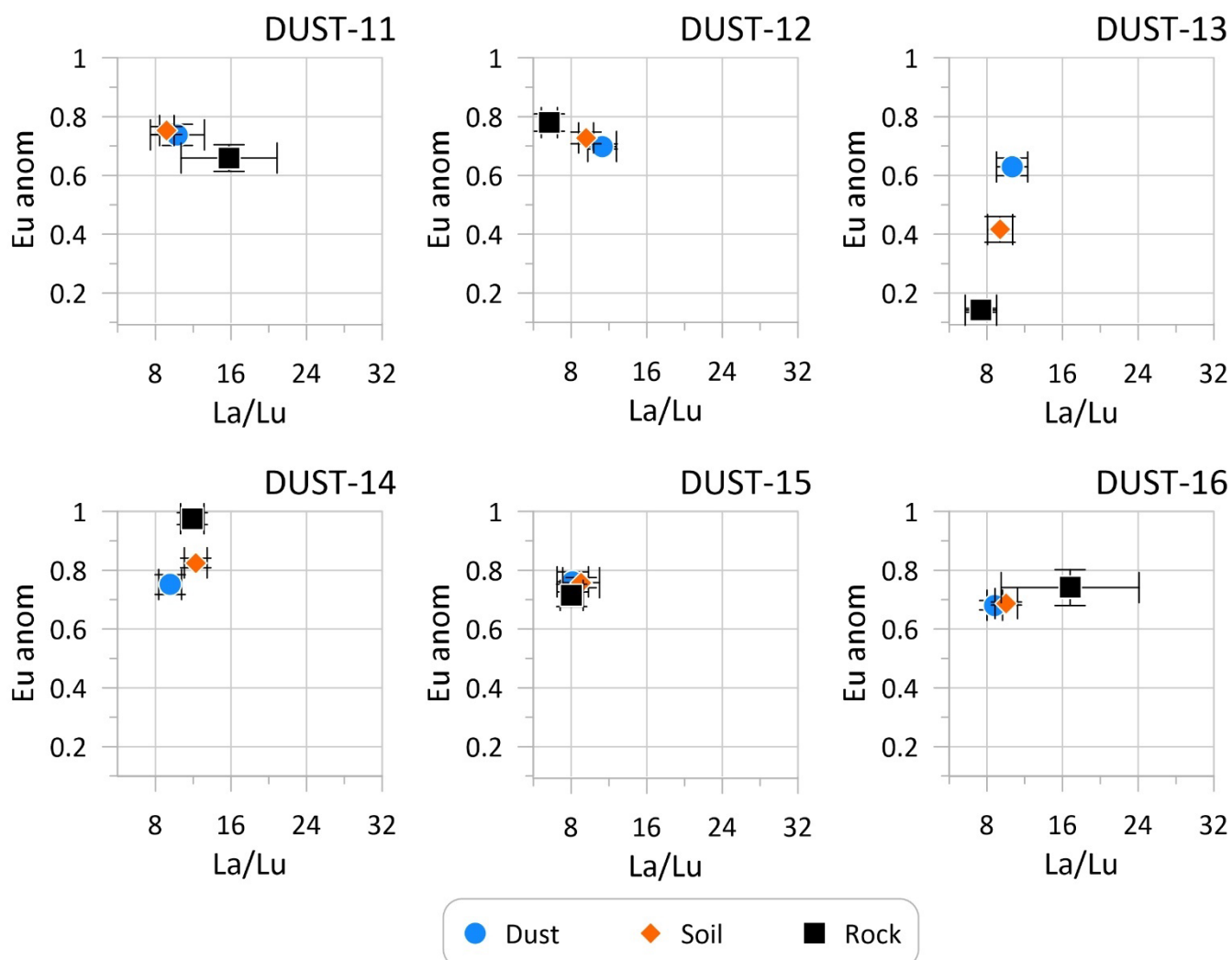
Figure 8. Biplot of La_n/Lu_n vs. Eu* at the six study sites. Symbols represent the mean ± 1 standard deviation.

355

Ratios of trace elements with limited mobility in surface environments are commonly employed to compare dust, soil, and local material (Muhs and Benedict, 2006; Mason and Jacobs, 1998; Reheis et al., 2002). In this study, the presence of different bedrock lithologies beneath the six study sites complicates the search for a single ratio appropriate for all locations. However, one ratio that is effective and appropriate given the results of Reynolds et al. (2010) is Cr/Ta. Because Cr is typically elevated in dust samples, but not apparently due to anthropogenic effects, and Ta is generally more abundant in soil, the Cr/Ta ratio can serve as an index of dust abundance within a given soil sample. At all sites, Cr/Ta is highest in dust samples (mean of 53.5 with a maximum of 66.5 at DUST-15) and lowest in rock samples (mean of 10.8 with a maximum of 13.8 at DUST-16). Soil samples have intermediate values, averaging 31.6.

As a final step to compare the sample types in terms of major elements, elemental abundances of Al, Ca, K, and Na were converted to oxide percent and used to calculate the chemical index of alteration-CIA (Nesbitt and Young, 1982) for dust, soil, and rock. This approach capitalizes on the tendency of CaO, K_2O and Na_2O to be leached by chemical weathering in surface environments, in contrast with the stability of Al_2O_3. Lower values indicate less weathered material, whereas progressive leaching drives the CIA toward higher values. The overall average of all samples in this study is 71.8, indicating a moderate degree of weathering. Notably, at all sites except DUST-14 the highest CIA values are found in the rock samples (mean of 75.8) and the lowest values in the dust (overall mean of 67.8). Moreover, the CIA for dust samples is very similar from site to site (standard deviation of 0.43), compared with the bedrock which varies widely (standard deviation of 5.74). Soil samples have generally intermediate values (mean of 73.7 ± 0.90).

4.4 Radiogenic Isotopes

Values of the $^{87}Sr/^{86}Sr$ ratio and ε_{Nd} provide an additional mechanism for distinguishing between dust, soil, and rock in this study (Table 4). Measured $^{87}Sr/^{86}Sr$ ratios average 0.71013 (0.70707 ± 0.00001 to 0.71423 ± 0.00001) for dust, 0.71076 (0.70863 ± 0.00001 to 0.71223 ± 0.00001) for soil, and 0.73629 (0.70476 ± 0.00001 to 0.76848 ± 0.00001) for rock. Values of ε_{Nd} average -8.92 (-11.37 ± 0.21 to -4.94 ± 0.22) for dust, -7.82 (-10.27 ± 0.15 to -6.20 ± 0.15) for soil, and -13.27 (-25.45 ± 0.15 to -4.51 ± 0.22) for rock. At each site, $^{87}Sr/^{86}Sr$ and ε_{Nd} are consistently similar for dust and soil samples, and more different for rock samples (Figure 9). At DUST-11, DUST-12, DUST-15, and DUST-16, values for dust and soil are nearly identical; at DUST-13 and DUST-14, there is slightly more separation between these materials. In general, values of dust and soil samples vary within a relatively narrow range between sites, whereas values for rock samples vary greatly (Figure 9).

4.5 Dust Fraction Estimates

Starting from the assumption that the soil samples from the locations considered in this study can logically be considered mixtures of local rock and eolian dust, the dust fraction (*fDust*) within each soil sample was estimated with a two end-member mixing model (Table 5). For this approach to function, end members need to be essentially unaffected by weathering within the CZ. However, given the different bedrock types present at each of the dust collector sites, and differences in the properties of dust delivered to each site, it is unlikely that a single pair of end members would work equally well for all 6 locations.

Collector	Sample name	Lab ID	$^{87}Sr/^{86}Sr$	2SE	$^{143}Nd/^{144}Nd$	2SE	$\varepsilon^{143}Nd$	2SE
Table 4. Radiogenic Isotope Results								
1	Dust-11 June 2021	22R-5	0.70906	0.00001	0.51224	0.00001	-7.72	0.18
1	Dust-11 Oct 2021	22R-12	0.70853	0.00001	0.51224	0.00001	-7.69	0.16
1	Dust 11	23R-1	0.70881	0.00001	0.51226	0.00001	-7.25	0.19
1	Soil 11	23R-7	0.70909	0.00001	0.51227	0.00001	-7.05	0.20
1	Rocks 11	23R-14	0.75782	0.00001	0.51159	0.00001	-20.39	0.15
2	Dust-12 June 2021	22R-6	0.71030	0.00001	0.51210	0.00001	-10.34	0.18
2	Dust-12 Oct 2021	22R-13	0.71002	0.00001	0.51210	0.00002	-10.35	0.35
2	Dust 12	23R-2	0.70978	0.00001	0.51207	0.00001	-10.93	0.16
2	Soil 12	23R-8	0.71165	0.00001	0.51215	0.00001	-9.48	0.17
2	Rocks 12	23R-15	0.75193	0.00001	0.51216	0.00001	-9.29	0.18
3	Dust-13 June 2021	22R-7	0.71100	0.00001	0.51212	0.00001	-9.98	0.19
3	Dust-13 Oct 2021	22R-14	0.71088	0.00001	0.51208	0.00001	-10.87	0.19
3	Dust 13	23R-3	0.71166	0.00001	0.51205	0.00001	-11.37	0.21
3	Soil 13	23R-9	0.71170	0.00001	0.51226	0.00001	-7.26	0.22
3	Rocks 13	23R-16	0.72302	0.00001	0.51238	0.00001	-5.01	0.15
4	Dust-14 Oct 2021	22R-15	0.71266	0.00001	0.51221	0.00001	-8.20	0.18
4	Dust 14	23R-4	0.71423	0.00001	0.51216	0.00001	-9.20	0.14
4	Soil 14	23R-11	0.71125	0.00001	0.51229	0.00001	-6.66	0.14
4	Rocks 14	23R-17	0.70476	0.00001	0.51240	0.00002	-4.51	0.36
5	Dust-15 Oct 2021	22R-16	0.70707	0.00001	0.51238	0.00001	-4.94	0.22
5	Dust 15	23R-5	0.70793	0.00001	0.51231	0.00002	-6.31	0.33
5	Soil 15	23R-12	0.70863	0.00001	0.51232	0.00001	-6.20	0.15
5	Rocks 15	23R-18	0.71171	0.00001	0.51187	0.00001	-14.95	0.14
6	Dust-16 Oct 2021	22R-17	0.71035	0.00001	0.51213	0.00001	-9.76	0.18
6	Dust 16	23R-6	0.70961	0.00001	0.51218	0.00002	-8.90	0.30
6	Soil 16	23R-13	0.71223	0.00001	0.51211	0.00001	-10.27	0.15
6	Rocks 16	23R-19	0.76848	0.00001	0.51133	0.00001	-25.45	0.15
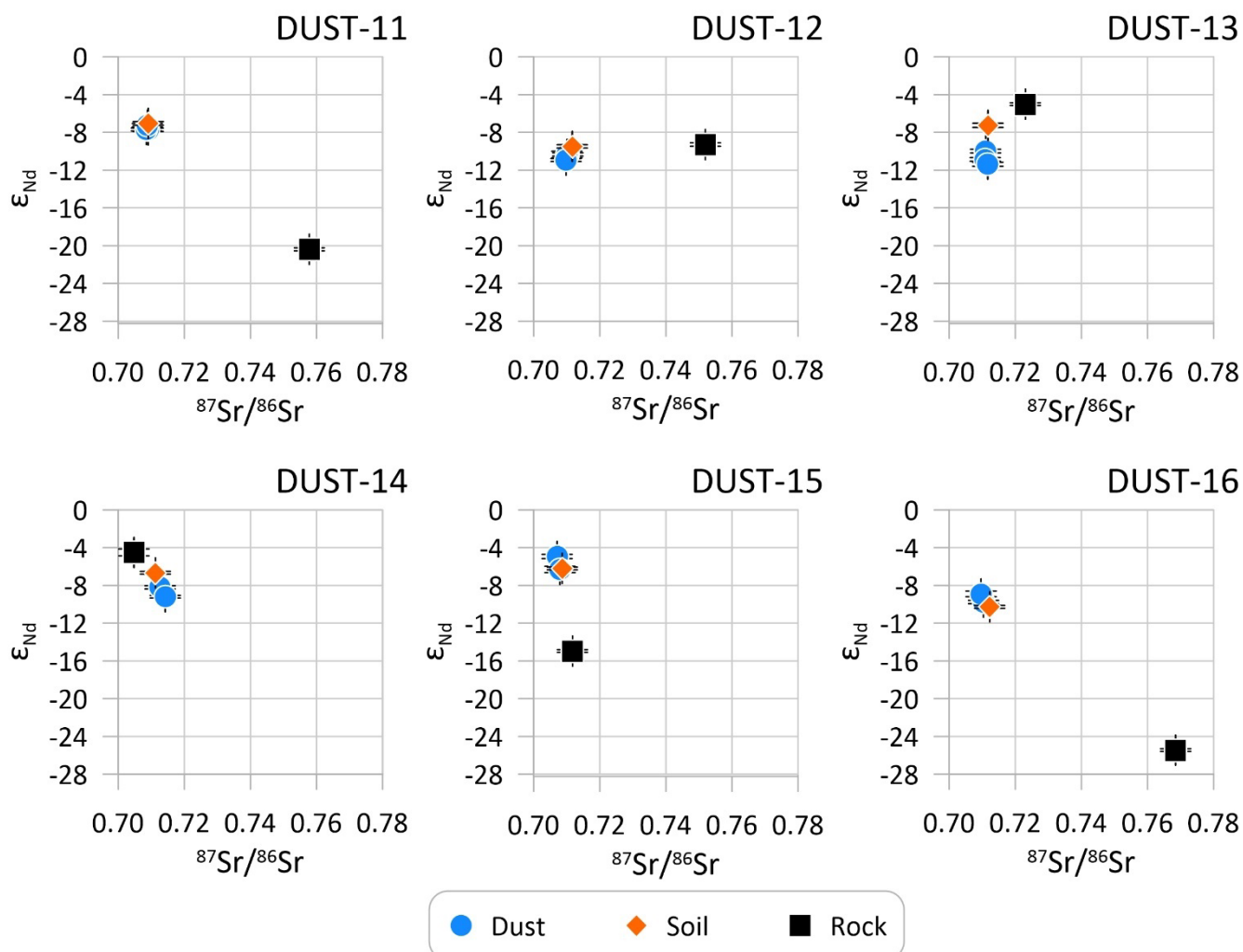
Figure 9. Biplots of $^{87}Sr/^{86}Sr$ and ε_{Nd} of soil, dust, and rock samples at the six study sites. Symbols represent the mean ± 1 standard error.

Accordingly, four pairs of end members were considered. Two of these utilize the radiogenic isotope results, since previous
395 work has demonstrated the applicability of $^{87}Sr/^{86}Sr$ and ε_{Nd} as fingerprints for geologic samples (e.g. Zhao et al., 2018).
Similarly, the ratio Cr/Ta was employed because Cr is generally more abundant in dust samples, and Ta is more common in
soil samples, allowing Cr/Ta to function as an index of dust content within the soil. In addition, the abundance of these
elements in regional dust was previously shown to have not changed in response to European settlement (Reynolds et al.,
2010), providing confidence that the modern dust samples are not distinct from prehistoric dust at these locations in terms of
400 Cr and Ta concentrations. Finally, the feldspar/quartz ratio was used to capitalize on the XRD mineralogy (Litaor, 1987).

As expected, estimates of *fDust* vary within each site, as well as between sites. However, in all cases, soils are clearly a
mixture of dust and rock-derived material, typically with a dominance of dust. For example, as demonstrated in Figure 9, the
$^{87}Sr/^{86}Sr$ ratio of most soil samples is very similar to that of the dust sample from the corresponding collector. The
concentration-weighted mixing models for $^{87}Sr/^{86}Sr$ and ε_{Nd} yield varying estimates for *fDust* (Figures 10 and 11). At DUST-
405 11, dust content quantified by this approach is >90%. At DUST-12, *fDust* from $^{87}Sr/^{86}Sr$ is near 0.60, whereas the estimate
from ε_{Nd} is much lower (<0.10). Values at DUST-13 and 14 are intermediate, and at DUST-15 and 16, the *fDust* estimates
from $^{87}Sr/^{86}Sr$ are near 0.40, in contrast to ε_{Nd} which yields estimates ~0.75 (Figures 10 and 11, Table 5). Estimates of *fDust*
from the ratio Cr/Ta vary across a similar range, from a high of 0.68 at DUST-16 to a low of 0.13 at DUST-13, with a mean
of 0.48 (Figure 11). Finally, estimates obtained from the Feldspar/Quartz ratio extend from a high of 0.96 at DUST-14, to a
410 low of 0.29 at DUST-13, with a mean of 0.57 (Figure 11). The average of all *fDust* estimates is 0.56, with the lowest mean
values per site at DUST-12 (0.41) and DUST-13 (0.34), and the highest mean values at DUST-11 (0.70) and DUST-14 (0.72).

5. Discussion

This project was designed to evaluate the contribution of eolian dust to soil formation in the alpine critical zone across a range
of mountain locations. Through the collection and analysis of dust, soil, and rock samples, three complementary objectives
415 were targeted: 1) to characterize the mineralogy and geochemistry of dust, soil, and rock samples from the six study sites; 2)
to quantify the fraction of the soil at each site derived from dust; and 3) to evaluate whether the dust fraction is elevated at
sites underlain by less weatherable bedrock lithologies.

5.1 Comparison of Mineralogy and Geochemistry

The mineralogical and geochemical analyses conducted as part of this project provide the framework necessary for evaluating
420 the degree of similarity between the dust, soil, and rock samples at each site. X-ray diffraction clearly reveals that minerals
present in the dust, such as feldspars, mica, illite, and kaolinite, are abundant in the soils, even in situations where these
minerals are absent in the underlying bedrock (Figure 6). This contrast indicates that these minerals accumulate in the soil as
a result of dust deposition over time, with the implication that the mineralogy of these soils would be quite different in the
absence of dust deposition (Yaalon and Ganor, 1973). A similar causal connection between dust and soil mineralogy was
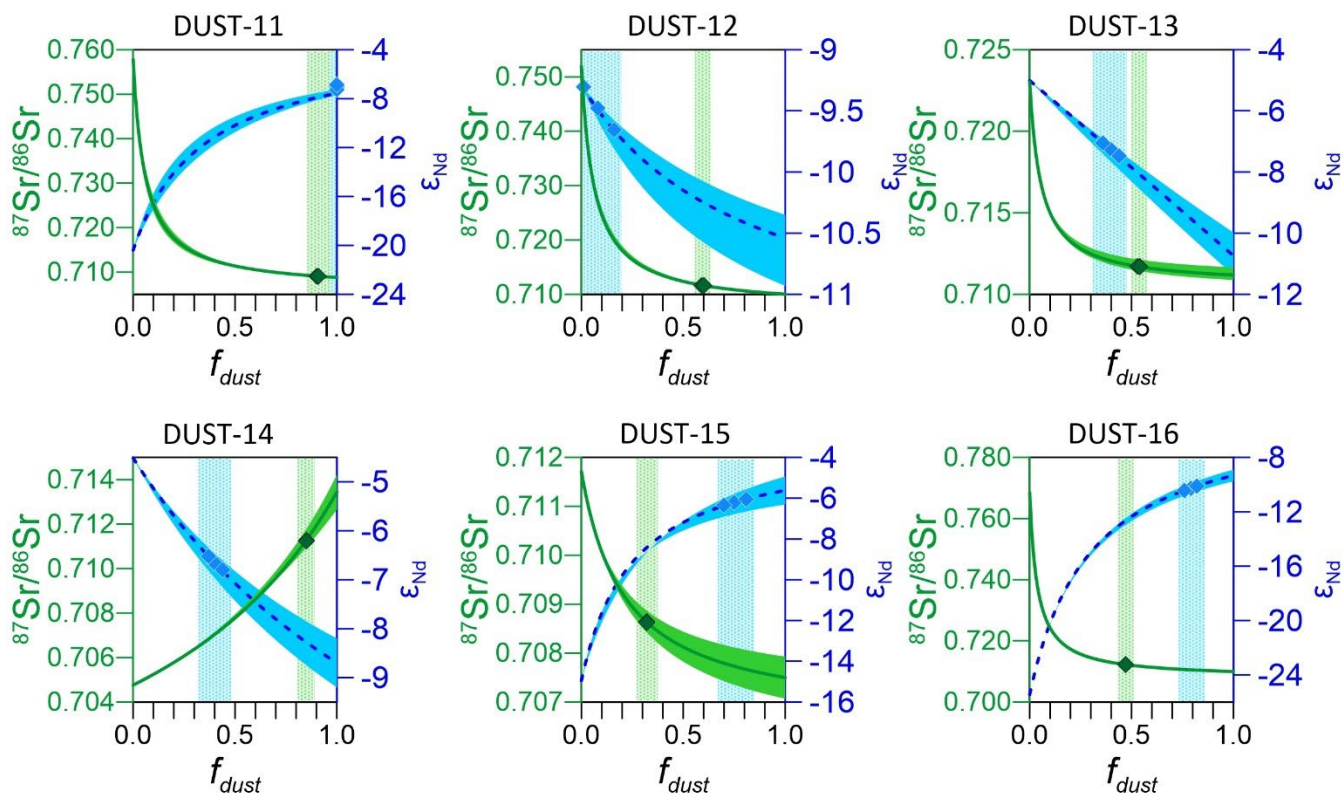
425

**Figure 10. Concentration-weighted mixing models used to estimate the dust fraction (*fDust*) in soil samples from measurements of
^{87}Sr/^{86}Sr and ε$_{Nd}$ at each of the six study sites. Green colours indicate ^{87}Sr/^{86}Sr whereas blue denotes ε$_{Nd}$. The width of the mixing
envelop reflects uncertainty in the analyses made on the dust and rock end members. The three diamonds in each plot indicate the
mean, mean – 1 standard error, and mean +1 standard error, of analyses made on the composite soil sample from each site. The**
430   **vertical green and blue shaded boxes are intended to visually highlight the *fDust* estimate range made at each site for ^{87}Sr/^{86}Sr and
ε$_{Nd}$.**
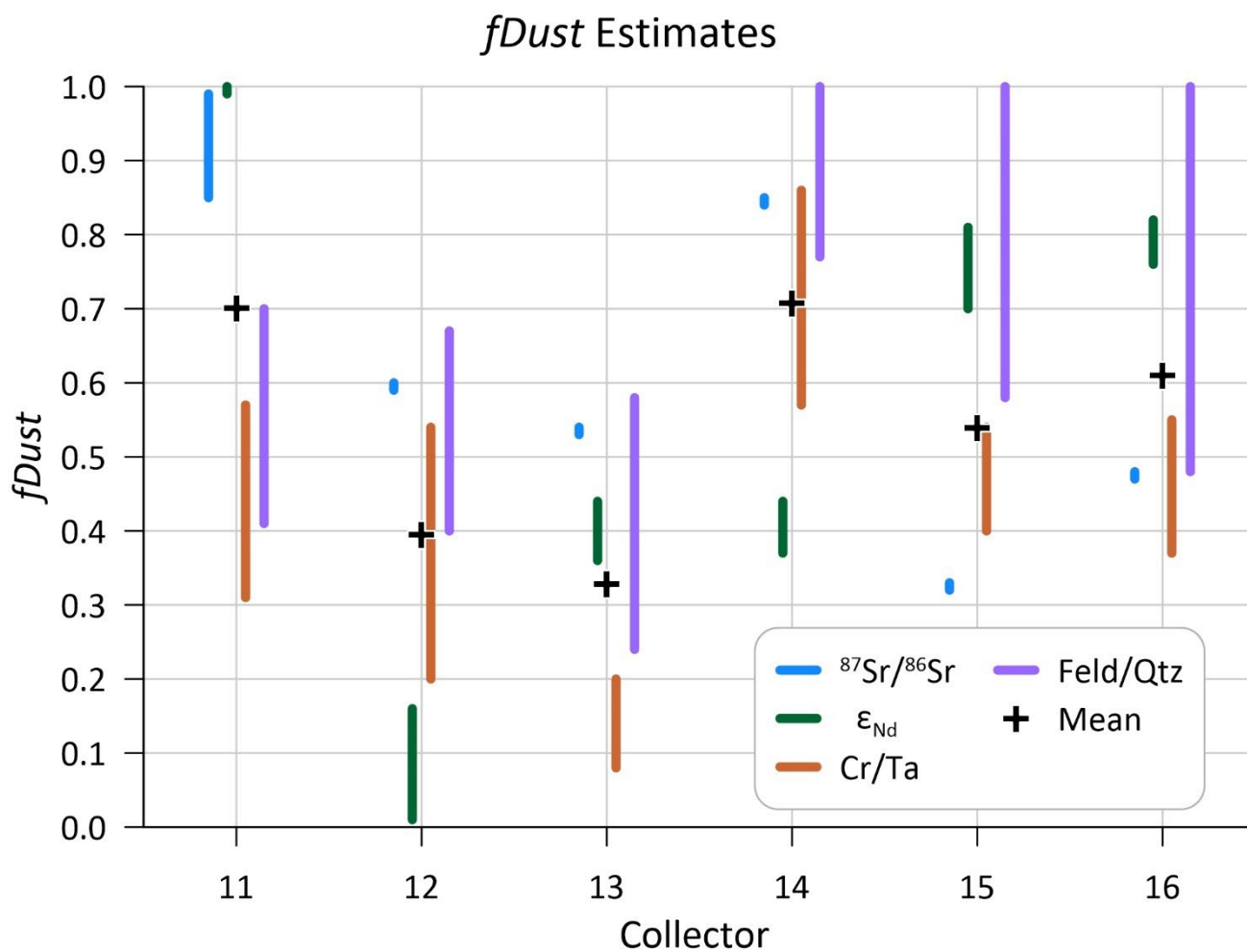
Figure 11. Summary of *fDust* estimates made at the six study sites with four mixing models: ^{87}Sr/^{86}Sr and ε$_{Nd}$, Cr/Ta, and Feld/Quartz. Vertical extent of each bar reflects the range of estimates for a given approach at a given site. The black crosses represent the overall mean at each site

435

Table 5. Dust Fraction Estimates								
Site	**^{87}Sr/^{86}Sr**		**ε_{Nd}**		**Cr/Ta**		**Feld/Qtz**	
	Mean	*Min, Max**	*Mean*	*Min, Max**	*Mean*	*Min, Max*	*Mean*	*Min, Max*
11	0.91	(0.85, 0.99)	1.00	(1.0^)	0.40	(0.31, 0.57)	0.49	(0.41, 0.70)
12	0.60	(0.59, 0.60)	0.08	(0.01, 0.16)	0.49	(0.20, 0.54)	0.49	(0.40, 0.67)
13	0.54	(0.53, 0.54)	0.40	(0.36, 0.44)	0.13	(0.08, 0.20)	0.29	(0.24, 0.58)
14	0.85	(0.85, 0.85)	0.40	(0.37, 0.44)	0.65	(0.57, 0.86)	0.96	(0.77, 1.00)
15	0.32	(0.32, 0.32)	0.75	(0.70, 0.81)	0.50	(0.40, 0.54)	0.63	(0.58, 1.0*)
16	0.47	(0.47, 0.47)	0.79	(0.76, 0.82)	0.68	(0.37, 0.55)	0.53	(0.48, 1.0*)

*Determined from ±1 SE of the measured soil value

^Rounded

reported for the mountain CZ in northern Utah (Munroe et al., 2015, 2021b), in Colorado (Lawrence et al., 2011; Litaor, 1987;
440 Birkeland et al., 2003), and in Wyoming (Dahms, 1993), as well as for mountain locations around the world such as Taiwan
(Tsai et al., 2021), Australia (Johnston, 2001), the Tibetan Plateau (Lin and Feng, 2015), and the Alps (Peer et al., 2022;
Grashey-Jansen et al., 2014; Küfmann, 2003).

The geochemical results reinforce the interpretation that soil composition has been impacted by dust deposition. At all
sites, the geochemistry of the soil samples more closely resembles that of the dust. This relationship is particularly obvious in
445 the results of principal component analysis (Figure 7). At the locations of DUST-11, 12, 15, and 16 the values for PC-1 and
PC-2 overlap for dust and soil, indicating that they are essentially identical. In contrast, values for the rock samples at these
sites plot far away in a non-overlapping field, indicating a great deal of dissimilarity. Further support comes from REEs
(Figure 8). Values of La_n/Lu_n in dust and soil are similar at all sites, whereas values in rock samples vary considerably. Values
of Eu* vary in a narrow range at DUST-11, 12, 15, and 16, but exhibit more spread at DUST-13 and DUST-14. Despite the
450 variability in rock samples, at all locations soil is similar to dust. Collectively, these patterns are consistent with soil formation
from a mixture of dust and rock, with a dominance of dust at most sites.

The abundance of trace elements in general provides another line of argument for the importance of dust deposition as a
control on the chemistry of these mountain soils. As noted previously, the abundances of most measured elements are higher
in dust and soil samples than in rock at each site. Ratios of elemental abundances dust/rock are >1.0 for nearly all measured
455 elements. The highest average dust/rock ratio is 212 for Sb, followed by 165 for Sn, 64 for P, 34 for Cu, 35 for Cd, and 31 for
Zn. Many of these elements were reported in previous studies to have abundances elevated above natural levels by
anthropogenic activity (Lawrence and Neff, 2009; Lawrence et al., 2010; Munroe, 2014; Heindel et al., 2020). Of the non-
anthropogenic elements reported by Reynolds et al. (2010), Ca exhibits the greatest enrichment in dust (25x) followed by Na,
Cr, Rb, and Ti, all with values ~4x. Notably, the abundance ratios dust/rock and soil/rock for the elements reported by
460 Reynolds et al. (2010) exhibit a significant positive correlation with an r^2 of 0.974 (P<0.001). Collectively these relationships
underscore that most elements are present in higher abundances in dust and soil compared with rock, and furthermore that
elements enriched to a higher level in dust tend to be enriched to a correspondingly higher level in soil.

Given their established utility as essentially immutable fingerprints, $^{87}Sr/^{86}Sr$ and ε_{Nd} provide a particularly strong
argument supporting the similarity of dust and soils in this study. As is clear from Figure 9, the isotopic fingerprints of the
465 dust collected at the different sites is consistent from season to season, and at DUST-11, 12, 15, and 16 they are
indistinguishable from the soil samples. At DUST-13 and 14, the soil sample plots in a more intermediate position between
dust and rock. In all cases, despite the wide ranging $^{87}Sr/^{86}Sr$ and ε_{Nd} of the rock samples, dust and soil samples generally plot
in the same region. This consistency is best explained if the soils contain a large amount of dust, and a correspondingly minor
contribution of weathered local bedrock.

470 As with the mineralogy results, the conclusion that dust deposition has impacted the abundances of major and trace
elements in these soils, along with $^{87}Sr/^{86}Sr$ and ε_{Nd}, is supported by studies of mountain soils from other locations. For
instance, in northern Utah, alpine soils over SiO_2-dominated quartzite bedrock were shown to be strongly controlled by

Quaternary dust deposition, with elemental chemistry and $^{87}Sr/^{86}Sr$ and ε_{Nd} of soil resembling dust and playa sources upwind, and strongly contrasting with local bedrock (Munroe et al., 2020). In Colorado, mountain soils demonstrate a clear

475 geochemical affinity with dust in their geochemistry and isotope fingerprint (Muhs and Benedict, 2006; Lawrence et al., 2013). In Idaho, ratios of immobile elements were shown to correspond between dust and soil (Ferrier et al., 2011). In Wyoming, the geochemistry of soils has changed as a result of the incorporation of Zr-poor eolian material over time (Reheis, 1990). In California, mountain soils in the Sierra Nevada have an isotope fingerprint that matches a mixture of Asian dust delivered by trans-Pacific transport and more regional material from California's Central Valley (Aciego et al., 2017). And in New Mexico,

480 gypsiferous dust derived from White Sand National Monument has a measurable impact on the chemistry and $^{87}Sr/^{86}Sr$ of soils positioned over sandstone in the Sacramento Mountains (Rea et al., 2020). Collectively, the mineralogical and geochemical results of this study clearly indicate that soils on these six widely distributed mountain summits have been strongly influenced by dust deposition, a finding that expands upon previous work focused on more limited spatial scales.

5.2 Dust Fraction in Soils

485 The conclusion that dust deposition plays a major role in controlling the mineralogy and geochemistry of the soils considered in this study leads naturally to the question of how much of the soil at each site is derived from dust deposition. Prior work from specific locations has yielded a range of estimates that form a context for the results presented here. For instance, in the San Juan Mountains of southwestern Colorado, mountain soils were estimated to contain 10 to 40% eolian dust, on the basis of $^{87}Sr/^{86}Sr$ and ε_{Nd} measurements (Lawrence et al., 2011). Values for *fDust* were generally higher for soils

490 over more resistant metamorphic bedrock, and were lower above less resistant volcanic rock. Following a similar isotope-based methodology, Munroe et al. (2020) estimated that alpine soils positioned over weathering-resistant quartzite in Utah contain 50 to 80% dust. Together, these studies indicate that the dust content in mountain soils can be large, and hint that the relative weatherability of the underlying bedrock can exert an influence on the magnitude of the dust component.

The range of *fDust* estimates generated in this study are consistent with this prior work (Figure 11, Table 5). It is not

495 possible to determine which of the approaches ($^{87}Sr/^{86}Sr$ and ε_{Nd}, Cr/Ta, or Feld/Quartz) is the most accurate, and given the varying bedrock lithologies, it should not be expected that one ratio would be equally appropriate at all sites. Therefore, an ensemble approach considering the range of estimates from all four ratios is considered prudent. With this in mind, the overall average estimate of 0.56 ± 0.24 (all four estimates at all six sites) is intermediate between the somewhat higher values over resistant quartzite in Utah and the lower values over more weatherable rock types in Colorado. Moreover, the lowest site

500 specific estimate (mean of 0.34) is over volcanic trachyte in the Tushar Mountains at DUST-13. In contrast, estimates are higher over quartzite bedrock at DUST-11, 15, and 16. This pattern supports the prediction that the importance of dust deposition to soil formation will be elevated at sites where the bedrock is weathering more slowly, and diminished in locations where the bedrock lithology is more vulnerable to weathering.

Estimates of *fDust* are less straightforward to interpret at DUST-12 and DUST-14. At DUST-12 the bedrock is quartzite,

505 which would support the expectation of a large dust component in the soils. However, *fDust* estimates at this site are actually

rather low, with a mean of 0.49. A significant factor is the very low (<0.10) value derived from ε_{Nd}. However, in contrast with the other sites, at DUST-12 there is very little spread in the values of ε_{Nd} between dust, soil, and rock (Figure 9). As a result, *fDust* estimates based on ε_{Nd} vary considerably (Table 5), and span an even wider array when the full error range is taken into account in the mixing model (Figure 10). As a result, the *fDust* value for DUST-12 is likely underestimated, and if the $^{87}Sr/^{86}Sr$ and ε_{Nd}-based estimates are discounted, then the overall estimate for DUST-12 overlaps with the values determined for the other sites underlain by quartzite (DUST-11, 15, and 16).

At DUST-14, the bedrock is trachyte similar to DUST-13, however the *fDust* estimates are higher. The value from ε_{Nd} is identical to the estimate (0.40) from the same technique for DUST-13. Yet counter-balancing that value is a very high estimate (0.96) from Feld/Quartz, and a high, but narrowly constrained (0.85), value from $^{87}Sr/^{86}Sr$. Both of these may relate to the bedrock at this site, which contains considerably more feldspar (Figure 6) than the other locations (mapped as hornblende plagioclase trachyte), has a Feld/Quartz ratio two orders of magnitude higher than the others (Table 3), and exhibits an unusually low $^{87}Sr/^{86}Sr$ ratio with relatively radiogenic ε_{Nd} (Figure 9). Rock samples from DUST-14 also have a much lower Rb/Sr ratio (0.2) than those at DUST-13 (23), reducing the potential for radiogenic ingrowth through decay of ^{87}Rb. These unique properties of the bedrock at DUST-14 may complicate attempts to compare results from this site with the other locations when calculated with the same methods. Furthermore, the dust at DUST-14 has a Feld/Quartz ratio notably low when compared with the other locations (Table 3), reflecting the preponderance of siliciclastic sedimentary rocks in the upwind region of the Colorado Plateau. Collectively these factors complicate efforts to constrain *fDust* at DUST-14, however it is nonetheless notable that the estimate from ε_{Nd} is low and identical at the two sites underlain by volcanic rocks.

5.3 Dust Influence on Pedogenesis

Together the mineralogy and geochemical results strongly support the conclusion that eolian dust is the dominant parent material for the alpine soils at the locations considered in this study. Therefore, it is a useful exercise to consider the soil texture and fertility in light of dust properties to evaluate how pedogenesis may have been directed by dust deposition. Perhaps the most straightforward connection relates to soil texture. At all sites, regardless of the nature of the underlying bedrock, nearly all of the sampled soils have silt loam textures, with total silt averaging 70% (Table 2). Silt, particularly in the very fine silt class (2-7 um), is also the most abundant grain size in the dust samples from these locations (Munroe et al., in review). This correspondence is consistent with eolian silt as the main parent material for these soils, and matches previous studies that compared dust and soil grain size distributions in mountain settings (Lawrence et al., 2011; Munroe et al., 2020; Litaor, 1987).

Soil grain size also corresponds with bedrock lithology, and the assessment of dust importance at each site presented above. The coarsest soils are at DUST-13 and DUST-14, where sand content averages 30% and total silt drops to 60% (Table 2). This pattern is consistent with a larger contribution of coarse material from physically weathered bedrock at these locations where the trachyte lithology should be less resistant than the metamorphic quartzite present at the other sites.

Statistical analysis reveals that the average amount of extractable Ca in the soils is strongly and positively correlated with the average amount of mineral Ca in the dust, and base saturation in these soils is dominated by Ca (Table 2). As noted above, ratios of elemental abundance in dust/rock and soil/rock reveal that Ca content is greatly elevated in the dust, an observation

540 corroborated by previous work (Munroe et al., 2021a). The wet technique used in this study to remove dust from the collectors might dissolve fine-grained calcite, making it difficult to assess whether calcite is present in the dust, as reported in previous studies (Litaor, 1987). However, XRD does demonstrate that Ca-bearing minerals such as plagioclase feldspar are present in all of the dust samples. Therefore, it seems likely that dust is delivering Ca to these soils in mineral form, and that weathering is releasing Ca to become plant-available. This same mechanism was invoked to explain the high Ca content of alpine soils

545 in the Uinta Mountains of Utah (Bockheim et al., 2000) and in the Colorado Rockies (Litaor, 1987).

Extractable K and Mg in the soil samples are significantly, and positively, correlated with the abundance of silt, with correlation coefficients of (P<0.001) 0.639 and 0.527 (P<0.001) respectively. Surprisingly, there is no significant relation between the amount of extractable K and Mg, and the abundance of these elements in mineral form in either dust or soil. This result could indicate that extractable K and Mg are delivered to soils in a plant-available form, perhaps adsorbed onto clay

550 minerals that XRD analysis demonstrates are present in the dust (Figure 6). At the same time, the apparent lack of a correlation between extractable K and Mg and their abundances in the dust may simply be an artefact of the limitations inherent in conducting statistical analysis on a small number of samples (average values from six sites).

Other aspects of the soil properties presented in Figure 5 can also be connected back to the conditions of each site and its regional position. Values of pH are generally highest at DUST-11 and 12 (Figure 5); these two sites are located farthest to the

555 southwest (Figure 1), and closest to the dry playas of the central Great Basin, suggesting that they might be positioned to receive larger amounts of carbonate and evaporite minerals. In contrast, DUST-15 and 16 are located farthest to the northwest where they likely receive dust delivered from the igneous terrane of the Snake River Plain that could be less able to counteract natural sources of acidity. Organic matter abundance is highest at DUST-15 (Figure 5), however this relatively low elevation site is the only one where (dwarf) trees are present in the vicinity of the collector. Thus, soils at this location could contain

560 higher amounts of organic matter due to greater abundance of vegetation now and in the past. The two unusually high values of extractable P at DUST-12 were the two samples collected from beneath vegetation (as opposed to from barren ground). Therefore, it may be that biochemical cycling at these micro-sites concentrated P, or conversely that these locations are vegetated as a consequence of elevated P abundance. Finally, CEC is significantly correlated (r=0.376, P=0.026) with the abundance of silt, matching the connecting between silt and extractable K and Mg noted earlier.

565 Collectively the mountain soils considered in this study are shallow, stony, and exhibit weak horizonation. Given their locations, they are also cold and spend much of the year frozen. Nonetheless, they are surprisingly fertile (Table 2), with circumneutral pH values, organic matter abundance averaging 6%, abundant plant-available Ca, K, and Mg, and cation exchange capacities similar to high-quality agricultural fields (Holmgren et al., 1993). That these soils exhibit such high fertility cannot be traced back to their underlying bedrock, which at four of the six sites is quartzite, and at all sites should be

570 weathering slowly given their periglacial climates. Instead, the properties of these soils can best be explained as a result of

long-term dust additions, corroborating conclusions from previous site-specific investigations of alpine soils (Bockheim et al., 2000; Litaor, 1987; Birkeland et al., 2003).

5.4 Implications

575   The results presented here clearly establish that the alpine soils considered in this study are a product of eolian dust deposition. Much of the silt content in these soils, which relates to their water holding capacity (Petersen et al., 1968), absolute surface area (Lawrence et al., 2011), and their ability to accommodate plant roots (Catt, 2001), has apparently been delivered as eolian material. Similarly, their notably high levels of plant-available nutrients can be traced back to the mineralogy and geochemistry of the dust they receive, rather than to weathering of the underlying bedrock (Aciego et al., 2017). The wide

580 spatial scale of the network of dust collectors employed in this work (Figure 1) represents a significant advance beyond the site-specific focus of previous projects, and firmly establish that the mountain CZ across a wide swath of southwestern North America has been profoundly influenced by long-term dust deposition. Simply stated, alpine soils in this region would not be what they are were it not for the dust they have accumulated over time.

     The primary implication of this conclusion is that future changes in dust flux will have corresponding effects on future

585 soil formation in the mountain CZ. Studies utilizing lake sediment archives have demonstrated that dust fluxes to parts of the Rocky Mountains have changed during the Holocene, likely in response to climatic factors (Arcusa et al., 2020; Routson et al., 2016, 2019; Munroe et al., 2021a), so dust flux should not be expected to be invariant. This realization is concerning for two reasons. First, dust delivery rates increased massively in response to European settlement in the southwestern US, underscoring the connection between human activity in the lowlands, and dust delivery to downwind mountain ecosystems

590 (Neff et al., 2008). As the population continues to grow in this region, which is home to some of the fastest growing cities in the United States (Wu et al., 2011), land-surface disturbance leading to increased dust emissions is almost unavoidable (Duniway et al., 2019; Belnap, 1995). Second, climate models predict that the arid parts of southwestern North America are likely to become even drier in the future (Cayan et al., 2010; Cook et al., 2015; Seager et al., 2013, 2007), and analysis of a 10-year dust deposition record in the Uinta Mountains confirms that greater aridity in the southwestern US corresponds to higher rates of dust deposition in downwind mountains (Munroe, 2022). Collectively, these insights support the prediction

595 that dust fluxes to the mountain CZ in this region are likely to remain high, and possibly increase, in the future. This change could affect mountain soils and the geoecological systems they support in a variety of ways, both positive and negative.

     An additional concern pertains to the elevated trace element abundances in modern dust. Analysis of modern dust and lake sediment records has demonstrated that many elements, including heavy metals of environmental concern such as As, Cu,

600 Cd, Mo, Pb, and Zn, are present at levels greatly in excess of their normal crustal values (Lawrence et al., 2010; Heindel et al., 2020; Munroe, 2014), and that many of these began to increase in abundance in concert with European settlement in the 19th Century and the start of widespread mining, smelting, and land-surface alteration in the drylands of southwestern North America (Reynolds et al., 2010; Munroe et al., 2015). Corresponding to their high abundances in dust, many trace metals are

also present at elevated abundances in alpine soils, as noted here and in previous work (Lawrence et al., 2013). It remains

605 unclear whether trace metals are accumulating in alpine soils to levels high enough to have environmental consequences (Lawrence et al., 2013), however, studies have demonstrated that the deposition of dust-derived metals has begun to impact sensitive mountain hydrologic systems (Moser et al., 2010). The question of whether these soils are being negatively impacted by trace-element loading remains open and should be investigated by future studies.

6. Conclusion

610 At six mountain sites in the southwestern United States, the mineralogy, geochemistry, and radiogenic isotope fingerprint of soils is very similar to modern dust, and consistently divergent from the local bedrock. This relationship is evidence that soils in the mountain critical zone (CZ) across this broad region are strongly influenced by the deposition of eolian material. This dust deposition controls soil texture and delivers minerals not present in the local bedrock, with corresponding effects on moisture holding capacity and fertility. This dust is also delivering heavy metals that are accumulating in the soils. Projections

615 of increasing aridity and anthropogenic land-surface disturbance in this region suggest that soils of the mountain CZ will be influenced by dust deposition to an even greater degree in the future. This causal connection between land-use at low elevations, and functioning of the mountain CZ, should be taken into account when designing land management strategies for arid landscapes subject to a variety of development pressures.

Acknowledgments

620 The authors thank S. Lusk, D. Munroe, and E. Norris for their help in the field, and C. Kluetmeier for assistance in the laboratory. The dust collectors were built by E. McMahon at Middlebury College. This work was supported by the US National Science Foundation [EAR-2012082] and by Middlebury College. Fieldwork took place in the ancestral homelands of the Goshute, Shoshone, and Ute tribes.

Data Availability

625 The data compiled in this study are available in the EarthChem Library at https://doi.org/10.26022/IEDA/113001 (dust chemistry 2021-2022), https://doi.org/10.26022/IEDA/113002 (soil and rock chemistry), and https://doi.org/10.26022/IEDA/112309 (dust chemistry 2020-2021).

Author Contributions

630   JSM conceived the project, acquired the funding, developed the methodology, conducted the investigations, administered the project, analysed the results, conducted the data visualization, and wrote the manuscript. AAS, EJS, and MJT participated in the analyses. All authors were involved in revising the manuscript for submission.

Competing Interests

The authors declare no competing interests

635 **References Cited**

Aciego, S. M., Riebe, C. S., Hart, S. C., Blakowski, M. A., Carey, C. J., Aarons, S. M., Dove, N. C., Botthoff, J. K., Sims, K. W. W., and Aronson, E. L.: Dust outpaces bedrock in nutrient supply to montane forest ecosystems, Nature Communications, 8, 14800, 2017.

Arcusa, S. H., McKay, N. P., Routson, C. C., and Munoz, S. E.: Dust-drought interactions over the last 15,000 years: A network 640 of lake sediment records from the San Juan Mountains, Colorado, The Holocene, 30, 559–574, 2020.

Arvin, L. J., Riebe, C. S., Aciego, S. M., and Blakowski, M. A.: Global patterns of dust and bedrock nutrient supply to montane ecosystems, Science Advances, 3, eaao1588, 2017.

Belnap, J.: Surface disturbances: Their role in accelerating desertification, Environ Monit Assess, 37, 39–57, https://doi.org/10.1007/BF00546879, 1995.

645 Birkeland, P. W., Shroba, R. R., Burns, S. F., Price, A. B., and Tonkin, P. J.: Integrating soils and geomorphology in mountains—an example from the Front Range of Colorado, Geomorphology, 55, 329–344, 2003.

Bockheim, J., Munroe, J., Douglass, D., and Koerner, D.: Soil development along an elevational gradient in the southeastern Uinta Mountains, Utah, USA, Catena, 39, 169–185, 2000.

Brantley, S. L., Goldhaber, M. B., and Ragnarsdottir, K. V.: Crossing disciplines and scales to understand the critical zone, 650 Elements, 3, 307–314, 2007.

Capo, R. C., Stewart, B. W., and Chadwick, O. A.: Strontium isotopes as tracers of ecosystem processes: theory and methods, Geoderma, 82, 197–225, 1998.

Catt, J. A.: The agricultural importance of loess, Earth-Science Reviews, 54, 213–229, https://doi.org/10.1016/S0012-8252(01)00049-6, 2001.

655 Cayan, D. R., Das, T., Pierce, D. W., Barnett, T. P., Tyree, M., and Gershunov, A.: Future dryness in the southwest US and the hydrology of the early 21st century drought, Proceedings of the National Academy of Sciences, 107, 21271–21276, 2010.

Colville, E. J., Carlson, A. E., Beard, B. L., Hatfield, R. G., Stoner, J. S., Reyes, A. V., and Ullman, D. J.: Sr-Nd-Pb Isotope Evidence for Ice-Sheet Presence on Southern Greenland During the Last Interglacial, Science, 333, 620–623, https://doi.org/10.1126/science.1204673, 2011.

660 Cook, B. I., Ault, T. R., and Smerdon, J. E.: Unprecedented 21st century drought risk in the American Southwest and Central Plains, Science Advances, 1, e1400082, 2015.

Crouvi, O., Pelletier, J. D., and Rasmussen, C.: Predicting the thickness and aeolian fraction of soils in upland watersheds of the Mojave Desert, Geoderma, 195, 94–110, 2013.

Dahms, D. E.: Mineralogical evidence for eolian contribution to soils of late Quaternary moraines, Wind River Mountains, 665 Wyoming, USA, Geoderma, 59, 175–196, 1993.

Derry, L. A. and Chadwick, O. A.: Contributions from Earth's atmosphere to soil, Elements, 3, 333–338, 2007.

Dixon, J. C. and Thorn, C. E.: Chemical weathering and landscape development in mid-latitude alpine environments, Geomorphology, 67, 127–145, 2005.

Duniway, M. C., Pfennigwerth, A. A., Fick, S. E., Nauman, T. W., Belnap, J., and Barger, N. N.: Wind erosion and dust from
670   US drylands: a review of causes, consequences, and solutions in a changing world, Ecosphere, 10, e02650, 2019.

Faure, G.: Principles and applications of geochemistry, Prentice Hall Upper Saddle River, NJ, 1997.

Ferrier, K. L., Kirchner, J. W., and Finkel, R. C.: Estimating millennial-scale rates of dust incorporation into eroding hillslope
regolith using cosmogenic nuclides and immobile weathering tracers, Journal of Geophysical Research: Earth Surface, 116,
2011.

675   Grashey-Jansen, S., Korch, O., Beck, C., Friedmann, A., Bernhard, R., and Dubitzky, C.: Aeolian influenced soil sites in
consideration of atmospheric circulation types–a case study in the alpine zone of the Zugspitzplatt (Northern Calcareous Alps,
Germany), Journal of Geology, Agriculture and Environmental sciences, 2, 11–19, 2014.

Graustein, W. C. and Armstrong, R. L.: The use of strontium-87/strontium-86 ratios to measure atmospheric transport into
forested watersheds, Science, 219, 289–292, 1983.

680   Greilinger, M. and Kasper-Giebl, A.: Saharan Dust Records and Its Impact in the European Alps, in: Oxford Research
Encyclopedia of Climate Science, 2021.

Hagedorn, F., Mulder, J., and Jandl, R.: Mountain soils under a changing climate and land-use, Biogeochemistry, 97, 1–5,
2010.

Heindel, R. C., Putman, A. L., Murphy, S. F., Repert, D. A., and Hinckley, E.-L. S.: Atmospheric Dust Deposition Varies by
685   Season and Elevation in the Colorado Front Range, USA, Journal of Geophysical Research: Earth Surface, 125,
e2019JF005436, https://doi.org/10.1029/2019JF005436, 2020.

Hirmas, D. R. and Graham, R. C.: Pedogenesis and soil-geomorphic relationships in an arid mountain range, Mojave Desert,
California, Soil Science Society of America Journal, 75, 192–206, 2011.

Holmgren, G. G. S., Meyer, M. W., Chaney, R. L., and Daniels, R. B.: Cadmium, lead, zinc, copper, and nickel in agricultural
690   soils of the United States of America, Wiley Online Library, 1993.

Hose, R. K. and Blake Jr, M. C.: Geology and mineral resources of White Pine County, Nevada, University of Nevada, 1976.

Huggett, R. J.: Soil landscape systems: a model of soil genesis, Geoderma, 13, 1–22, 1975.

Hunt, C. B. and Waters, A. C.: Structural and igneous geology of the La Sal Mountains, Utah, US Government Printing Office,
1958.

695   Jenny, H.: Factors of soil formation: a system of quantitative pedology, McGraw-Hill New York, 1983.

Jochum, K. P., Weis, U., Schwager, B., Stoll, B., Wilson, S. A., Haug, G. H., Andreae, M. O., and Enzweiler, J.: Reference
Values Following ISO Guidelines for Frequently Requested Rock Reference Materials, Geostandards and Geoanalytical
Research, 40, 333–350, https://doi.org/10.1111/j.1751-908X.2015.00392.x, 2016.

Johnston, S. W.: The influence of aeolian dust deposits on alpine soils in south-eastern Australia, Soil Res., 39, 81–88,
700   https://doi.org/10.1071/sr99121, 2001.

Küfmann, C.: Soil types and eolian dust in high-mountainous karst of the Northern Calcareous Alps (Zugspitzplatt, Wetterstein
Mountains, Germany), Catena, 53, 211–227, 2003.

Lawrence, C. R. and Neff, J. C.: The contemporary physical and chemical flux of aeolian dust; a synthesis of direct measurements of dust deposition, Chem.Geol., 267, 46–63, https://doi.org/10.1016/j.chemgeo.2009.02.005, 2009.

705 Lawrence, C. R., Painter, T. H., Landry, C. C., and Neff, J. C.: Contemporary geochemical composition and flux of aeolian dust to the San Juan Mountains, Colorado, United States, Journal of Geophysical Research, 115, G03007, https://doi.org/10.1029/2009JG001077, 2010.

Lawrence, C. R., Neff, J. C., and Farmer, Gl.: The accretion of aeolian dust in soils of the San Juan Mountains, Colorado, USA, Journal of Geophysical Research -- Earth Surface, 116, F02013, https://doi.org/10.1029/2010JF001899, 2011.

710 Lawrence, C. R., Reynolds, R. L., Ketterer, M. E., and Neff, J. C.: Aeolian controls of soil geochemistry and weathering fluxes in high-elevation ecosystems of the Rocky Mountains, Colorado, Geochim.Cosmochim.Acta, 107, 27–46, 2013.

Lin, Y.-C. and Feng, J.-L.: Aeolian dust contribution to the formation of alpine soils at Amdo (Northern Tibetan Plateau), Geoderma, 259–260, 104–115, https://doi.org/10.1016/j.geoderma.2015.05.012, 2015.

Litaor, M. I.: The influence of eolian dust on the genesis of alpine soils in the Front Range, Colorado, Soil Sci.Soc.Am.J., 51, 715 142–147, 1987.

Litherland, M. M. and Klemperer, S. L.: Crustal structure of the Ruby Mountains metamorphic core complex, Nevada, from passive seismic imaging, Geosphere, 13, 1506–1523, 2017.

Mason, J. A. and Jacobs, P. M.: Chemical and particle-size evidence for addition of fine dust to soils of the midwestern United States, Geology, 26, 1135–1138, 1998.

720 Miller, D. M.: Structural geology of the northern Albion Mountains, Geol Soc Am Mem, 153, 399–423, 1980.

Moser, K. A., Mordecai, J. S., Reynolds, R. L., Rosenbaum, J. G., and Ketterer, M. E.: Diatom changes in two Uinta mountain lakes, Utah, USA: responses to anthropogenic and natural atmospheric inputs, Hydrobiologia, 648, 91–108, 2010.

Muhs, D. R. and Benedict, J. B.: Eolian additions to late Quaternary alpine soils, Indian Peaks Wilderness Area, Colorado Front Range, Arct.Antarct.Alp.Res., 38, 120–130, 2006.

725 Munroe, J. S.: Properties of modern dust accumulating in the Uinta Mountains, Utah, USA, and implications for the regional dust system of the Rocky Mountains, Earth Surf.Process.Landforms, 39, 1979–1988, 2014.

Munroe, J. S.: Relation between regional drought and mountain dust deposition revealed by a 10-year record from an alpine critical zone, Science of The Total Environment, 844, 156999, 2022.

Munroe, J. S., Attwood, E. C., O'Keefe, S. S., and Quackenbush, P. J.: Eolian deposition in the alpine zone of the Uinta 730 Mountains, Utah, USA, Catena, 124, 119–129, 2015.

Munroe, J. S., Norris, E. D., Olson, P. M., Ryan, P. C., Tappa, M. J., and Beard, B. L.: Quantifying the contribution of dust to alpine soils in the periglacial zone of the Uinta Mountains, Utah, USA, Geoderma, 378, 114631, 2020.

Munroe, J. S., McElroy, R., O'Keefe, S., Peters, A., and Wasson, L.: Holocene records of eolian dust deposition from high-elevation lakes in the Uinta Mountains, Utah, USA, Journal of Quaternary Science, 36, 66–75, 2021a.

735 Munroe, J. S., Ryan, P. C., and Proctor, A.: Pedogenic clay formation from allochthonous parent materials in a periglacial alpine critical zone, Catena, 203, 105324, 2021b.

Nakamura, N.: Determination of REE, Ba, Fe, Mg, Na and K in carbonaceous and ordinary chondrites, Geochimica et Cosmochimica Acta, 38, 757–775, 1974.

740 Neff, J. C., Ballantyne, A. P., Farmer, G. L., Mahowald, N. M., Conroy, J. L., Landry, C. C., Overpeck, J. T., Painter, T. H., Lawrence, C. R., and Reynolds, R. L.: Increasing eolian dust deposition in the western United States linked to human activity, Nature Geoscience, 1, 189–195, https://doi.org/10.1038/ngeo133, 2008.

Nesbitt, Hw. and Young, G. M.: Early Proterozoic climates and plate motions inferred from major element chemistry of lutites, nature, 299, 715–717, 1982.

Osborn, G. and Bevis, K.: Glaciation in the Great Basin of the Western United States, Quaternary Science Reviews, 20, 1377–
745 1410, 2001.

Peer, T., Zheng, L.-J., Neubauer, F., Friedl, G., Hauzenberger, C., and Kasper-Giebl, A.: Mineralogical Composition and Origin of Airborne Dust in an Alpine Environment of Hochtor (Hohe Tauern, Austria): Effects on Pedogenesis, Biological Soil Crusts, and Vascular Plant Growth, Frontiers in Earth Science, 10, 2022.

Petersen, G. W., Cunningham, R. L., and Matelski, R. P.: Moisture characteristics of Pennsylvania soils: II. Soil factors
750 affecting mositure retention within a textural class—silt loam, Soil Science Society of America Journal, 32, 866–870, 1968.

Pourmand, A., Prospero, J. M., and Sharifi, A.: Geochemical fingerprinting of trans-Atlantic African dust based on radiogenic Sr-Nd-Hf isotopes and rare earth element anomalies, Geology, 42, 675–678, 2014.

Rea, P., Ma, L., Gill, T. E., Gardea-Torresdey, J., Tamez, C., and Jin, L.: Tracing gypsiferous White Sands aerosols in the shallow critical zone in the northern Sacramento Mountains, New Mexico using Sr/Ca and 87Sr/86Sr ratios, Geoderma, 372,
755 114387, 2020.

Reheis, M. C.: Influence of climate and eolian dust on the major-element chemistry and clay mineralogy of soils in the northern Bighorn Basin, USA, Catena, 17, 219–248, 1990.

Reheis, M. C. and Kihl, R.: Dust deposition in southern Nevada and California, 1984-1989: Relations to climate, source area, and source lithology, Journal of Geophysical Research.D.Atmospheres, 100, 8893–8918, 1995.

760 Reheis, M. C., Budahn, J. R., and Lamothe, P. J.: Geochemical evidence for diversity of dust sources in the southwestern United States, Geochimica et Cosmochimica Acta, 66, 1569–1587, 2002.

Reynolds, R. L., Mordecai, J. S., Rosenbaum, J. G., Ketterer, M. E., Walsh, M. K., and Moser, K. A.: Compositional changes in sediments of subalpine lakes, Uinta Mountains (Utah): evidence for the effects of human activity on atmospheric dust inputs, J.Paleolimnol., 44, 161–175, 2010.

765 Ross, M. L., Friedman, J. D., and Huffman, A. C.: Geology of the Tertiary intrusive centers of the La Sal Mountains, Utah—Influence of preexisting structural features on emplacement and morphology, in: Laccolith Complexes of Southeastern Utah: Tectonic Control and Time of Emplacement—Workshop Proceedings: US Geological Survey Bulletin, 61–83, 1998.

Routson, C. C., Overpeck, J. T., Woodhouse, C. A., and Kenney, W. F.: Three millennia of southwestern North American dustiness and future implications, PloS one, 11, e0149573, 2016.

770 Routson, C. C., Arcusa, S. H., McKay, N. P., and Overpeck, J. T.: A 4,500-Year-Long Record of Southern Rocky Mountain Dust Deposition, Geophysical Research Letters, 46, 8281–8288, https://doi.org/10.1029/2019GL083255, 2019.

Seager, R., Ting, M., Held, I., Kushnir, Y., Lu, J., Vecchi, G., Huang, H.-P., Harnik, N., Leetmaa, A., and Lau, N.-C.: Model projections of an imminent transition to a more arid climate in southwestern North America, Science, 316, 1181–1184, 2007.

775 Seager, R., Ting, M., Li, C., Naik, N., Cook, B., Nakamura, J., and Liu, H.: Projections of declining surface-water availability for the southwestern United States, Nature Climate Change, 3, 482–486, 2013.

Simonson, R. W.: Airborne dust and its significance to soils, Geoderma, 65, 1–43, 1995.

Singh, R., Gupta, I., Raina, R., Mahajan, P., Srivastava, P., Singh, V. K., and Batish, D. R.: Mountain soils and climate change: importance, threats and mitigation measures, in: Understanding Soils of Mountainous Landscapes, Elsevier, 3–21, 2023.

Steven, T. A.: Igneous activity and related ore deposits in the western and southern Tushar Mountains, Marysvale Volcanic
780 Field, west-central Utah, 1984.

Tang, Y., Han, G., Wu, Q., and Xu, Z.: Use of rare earth element patterns to trace the provenance of the atmospheric dust near Beijing, China, Environmental earth sciences, 68, 871–879, 2013.

Tito, R., Vasconcelos, H. L., and Feeley, K. J.: Mountain ecosystems as natural laboratories for climate change experiments, Frontiers in Forests and Global Change, 3, 38, 2020.

785 Tsai, H., Chen, J.-H., Huang, W.-S., Huang, S.-T., Hseu, Z.-Y., and You, C.-F.: Aeolian additions of podzolic soils on the high-altitude mountains in central Taiwan-sediment origin and pedological implications, Geoderma, 383, 114726, 2021.

Wu, J., Jenerette, G. D., Buyantuyev, A., and Redman, C. L.: Quantifying spatiotemporal patterns of urbanization: The case of the two fastest growing metropolitan regions in the United States, Ecological Complexity, 8, 1–8, 2011.

Yaalon, D. H. and Ganor, E.: The influence of dust on soils during the Quaternary, Soil Sci., 116, 146–155, 1973.

790 Zhao, W., Balsam, W., Williams, E., Long, X., and Ji, J.: Sr–Nd–Hf isotopic fingerprinting of transatlantic dust derived from North Africa, Earth and Planetary Science Letters, 486, 23–31, 2018.

Zheng, K., Li, Y., Li, Z., and Huang, J.: Provenance tracing of dust using rare earth elements in recent snow deposited during the pre-monsoon season from mountain glaciers in the central to northern Tibetan Plateau, Environmental Science and Pollution Research, 28, 45765–45779, 2021.

795